

A revised and expanded deep radiostratigraphy of the Greenland Ice Sheet from airborne radar sounding surveys between 1993–2019

Joseph A. MacGregor¹, Mark A. Fahnestock², John D. Paden³, Jilu Li³, Jeremy P. Harbeck⁴, Andy Aschwanden²

¹ Cryospheric Sciences Laboratory, NASA Goddard Space Flight Center, Greenbelt, Maryland, United States of America

² Geophysical Institute, University of Alaska Fairbanks, Fairbanks, Alaska, United States of America

³ Center for Remote Sensing and Integrated Systems, The University of Kansas, Lawrence, Kansas, United States of America

⁴ ADNET Systems, Bethesda, Maryland, United States of America

Correspondence to: Joseph A. MacGregor (joseph.a.macgregor@nasa.gov)

Abstract. Between 1993 and 2019, NASA and NSF sponsored 26 separate airborne campaigns that surveyed the thickness and radiostratigraphy of the Greenland Ice Sheet using successive generations of coherent VHF radar sounders developed and operated by The University of Kansas. Most of the ice-sheet’s internal VHF radiostratigraphy is composed of isochronal reflections that record its integrated response to past centennial-to-multi-millennial-scale climatic and dynamic events. We previously generated the first comprehensive dated radiostratigraphy of the Greenland Ice Sheet using the first 20 of these campaigns (1993–2013) and investigated its value for constraining the ice sheet’s history and modern boundary conditions. Here we describe the second version of this radiostratigraphic dataset using all 26 campaigns, which includes substantial improvements in survey coverage and was mostly acquired with higher-fidelity systems. We improved quality control and accelerated reflection tracing and matching by including an automatic test for stratigraphic conformability, a thickness-normalized reprojection for radargrams, and automatic inter-segment reflection matching. We reviewed and augmented the 1993–2013 radiostratigraphy, and we applied an existing independently developed method for predicting radiostratigraphy to the previously untraced campaigns (2014–2019) to accelerate their semi-automatic tracing. The result is a more robust radiostratigraphy and age structure of the ice sheet that covers up to 65% of the ice sheet and includes >58 600 km of newly traced reflections from the 2014–2019 campaigns. This dataset can be used to validate the sensitivity of ice-sheet models to past major climate changes and constrain long-term boundary conditions (e.g., accumulation rate). Based on these results, we make several recommendations for how radiostratigraphy may be traced more efficiently and reliably in the future. This dataset is freely available at <https://doi.org/10.5281/zenodo.15132763> (MacGregor et al., 2025). It includes all traced reflections at the spatial resolution of the radargrams and grids (5 km horizontal resolution) of the depths of isochrones between 3–115 ka and ages between 10–80% of the ice thickness; associated codes are available at <https://doi.org/10.5281/zenodo.14183061> (MacGregor, 2024a).

Deleted: major

Deleted: incorporated several lessons learned from our previous efforts for

Deleted: ,

Deleted: a cutoff length for semi-automatic tracing propagation, ...

Deleted: 14531734

Deleted: 4

38 **1 Introduction**

39 The Greenland Ice Sheet (*GrIS*) is losing mass rapidly and is projected to do so for the foreseeable future unless substantial
40 mitigation of anthropogenic warming is undertaken (Aschwanden et al., 2019; Goelzer et al., 2020; Otosaka et al., 2023). Ice-
41 sheet models are the essential tools used to make these projections, but the uncertainty in these projections is large and
42 significantly affects how society might respond to the global and regional sea-level change caused by GrIS wastage
43 (Aschwanden et al., 2021). Numerous efforts are underway to reduce this uncertainty (e.g., Aschwanden and Brinkerhoff,
44 2022), and among the major challenges that these efforts seek to address are the initialization of these models prior to applying
45 projected external forcings (typically atmospheric and oceanic) and whether their long-term sensitivity to anthropogenic
46 climate change is consistent with that inferred from paleoclimatic records (e.g., Goelzer et al., 2018; Briner et al., 2020).
47 Fortunately, the GrIS contains within itself a substantial and spatially well-distributed archive of its integrated response to past
48 climate change: its isochronal radiostratigraphy. Further, this radiostratigraphy can constrain the subsurface state and dynamics
49 of the present-day GrIS in a manner not achieved by other spatially distributed observations; it is also potentially valuable for
50 identifying well-initialized instances of ice-sheet models (e.g., Bingham et al., in review).

51 MacGregor et al. (2015a) (hereafter *M15*) generated the first large-scale dated radiostratigraphy of the GrIS. That study
52 was made possible by the abundance of high-quality very high frequency (*VHF*) airborne-radar sounding data collected in the
53 prior two decades (1993–2013, all years CE) sponsored by the United States’ (*US*) National Aeronautics and Space
54 Administration (*NASA*) and National Science Foundation (*NSF*; CReSIS, 2024), advances in radar-sounder design led by The
55 University of Kansas (*KU*; e.g., Gogineni et al., 1998) and its Center for Remote Sensing and Integrated Systems (*CReSIS*;
56 e.g., Rodríguez-Morales et al., 2014; Arnold et al., 2020), and a suite of synchronized deep ice cores collected by international
57 consortiums led primarily by Denmark and the United States (e.g., Rasmussen et al., 2006; Dahl-Jensen et al., 2013; Seierstad
58 et al., 2014; Mojtabavi et al., 2020). *M15* introduced several advances in prediction, mapping, dating, validation and gridding
59 of radiostratigraphy to generate the first ice-sheet-wide age volume for either of Earth’s two remaining ice sheets. That study
60 enabled numerous improvements in mapping of key ice-sheet boundary conditions (e.g., MacGregor et al., 2015b, 2016a,b,
61 2022; Dow et al., 2018). It also motivated refinements to – and assessment of – methods for mapping and modeling
62 radiostratigraphy (e.g., Born, 2017; Xiong et al., 2018; Delf et al., 2020; Born and Robinson, 2021). However, no subsequent
63 study has significantly improved upon the *M15* dataset itself, either by infilling isochronal reflections that were unmapped by
64 *M15* or by incorporating the large quantity of additional similar airborne-radar sounding data collected as part of *NASA*’s
65 Operation IceBridge (*OIB*) in 2014–2019 that was not included in *M15* (MacGregor et al., 2021).

66 Here we describe version 2 (v2) of the GrIS radiostratigraphy dataset and the methods to generate it, with a particular
67 emphasis on methodological improvements introduced since *M15* and remaining uncertainties. Based on the development of
68 this dataset, we identify future opportunities for developing a more complete deep radiostratigraphy of the GrIS and make
69 recommendations for future improvements in tracing methods.

Deleted ;

Deleted: Rasmussen et al., 2013;

72 **2 Airborne radar-sounding data**

73 To build this second version of the GrIS-wide radiostratigraphy, we first evaluate the same 1993–2013 VHF radar-sounding
 74 data collected over the GrIS by KU/CReSIS as M15 used to generate v1 (Table 1; Fig. 1; CReSIS, 2024). We further consider
 75 the additional six OIB campaigns worth of VHF radar-sounding data collected annually during boreal springtime between
 76 2014–2019 by KU/CReSIS using identical or similar system configurations. These data were recorded coherently and
 77 subsequently focused using synthetic aperture radar (*SAR*) methods by KU/CReSIS. The nominal vertical resolution of these
 78 processed data is 2.5–4.4 m, which is sufficiently fine to resolve many (often dozens) distinct internal reflections, while their
 79 along-track resolution is more variable (~15–150 m depending on system and campaign). Depending on system performance,
 80 in-flight acquisition decisions and post-processing requirements, individual survey flights are composed of one or more
 81 *segments*, which can be tens to thousands of kilometers long depending on how many segments constitute each flight. Each
 82 segment is further divided into a sequence of ~50-km-long data *frames*, which are the format in which the data are distributed
 83 by KU/CReSIS. For example, the flight on 2011-05-02 (*20110502* in KU/CReSIS nomenclature), is divided into two segments,
 84 (*20110502_01* and *20110502_02*, respectively), which are composed of 38 and 35 frames, respectively (*20110502_01_001–*
 85 *20110502_01_038*, and *20110502_02_001–20110502_02_035*). We evaluate these SAR-focused data “as-is” and do not
 86 perform any substantive re-processing thereof, although we note that at least one focusing method has since been introduced
 87 that is intended to optimize detection of specular internal reflections (Castelletti et al., 2019).
 88

89 **Table 1:** NASA/NSF/KU/CReSIS airborne radar sounding surveys of the GrIS between 1993–2019 considered in this study.

Year	Aircraft type ^a	Radar sounder ^b	Priority rating ^c	Total length evaluated ^d		Length traced ^e				
				v1 (M15) (km)	v2 (this study) (km)	v1 (km)	v1 (%)	v2 (km)	v2 (%)	v2–v1 change (km)
1993	P-3B	ICORDS	Low	17 205	1 703	4 243	25	868	51	–3 375
1995	P-3B	ICORDS	Low	13 641	4 053	6 640	49	3 853	95	–2 787
1996	P-3B	ICORDS	Low	4 527	249	2 999	66	249	100	–2 750
1997	P-3B	ICORDS	Medium	14 123	5 885	5 922	42	4 019	68	–1 903
1998	P-3B	ICORDS v2	Medium	25 977	7 052	11 538	44	3 993	57	–7 545

1999	P-3B	ICORDS v2	Medium	33 993	26 493	24 409	72	20 458	77	-3 951
2001	P-3B	ICORDS v2	Medium	10 899	4 530	2 623	24	2 880	64	+257
2002	P-3B	ICORDS v2	Medium	21 187	9 137	10 642	50	7 100	78	-3 542
2003	P-3B	ACORDS	Medium	13 988	7 950	6 022	43	4 865	61	-1 157
2005	DHC-6	ACORDS	Low	6 096	0	761	12	0	0	-761
2006	DHC-6	MCRDS	Low	12 289	268	1 796	15	122	46	-1 674
2007	P-3B	MCRDS	Medium	11 846	4 303	2 192	19	1 791	42	-401
2008	DHC-6	MCRDS	Low	22 706	8 802	7 438	33	6 526	74	-912
2009	DHC-6	MCRDS	Low	9 250	366	341	4	323	88	-18
2010	DC-8	MCoRDS	Medium	25 186	10 370	3 677	15	3 543	34	-111
2010	P-3B	MCoRDS	Medium	28 171	2 547	2 840	10	1 027	40	-1 813
2011	P-3B	MCoRDS v2	High	74 875	31 192	25 814	34	20 987	67	-5 727
2011	DHC-6	MCRDS	Low	7 172	708	660	9	328	46	-332
2012	P-3B	MCoRDS v2	High	88 278	34 791	23 192	26	22 270	64	-472
2013	P-3B	MCoRDS v3	Medium	41 494	11 663	16 484	40	7 011	60	-9 473
2014	P-3B	MCoRDS v3	High	(88 893)	35 460	N/A		26 374	74	+26 374
2015	C-130H	MCoRDS v5	Medium	(71 291)	450	N/A		346	77	+346
2016	WP-3D	MCoRDS v5	Medium	(27 134)	250	N/A		248	99	+248
2017	P-3B	MCoRDS v3	High	(78 841)	19 805	N/A		13 229	67	+13 229
2018	P-3B	MCoRDS v3	Medium	(42 189)	2 000	N/A		1 397	70	+1 397
2019	P-3B	MCoRDS v3	Medium	(59 419)	18 732	N/A		17 016	91	+17 016
Total				482 902 (850 669)	248 758	160 233	N/A	170 823	N/A	+10 590

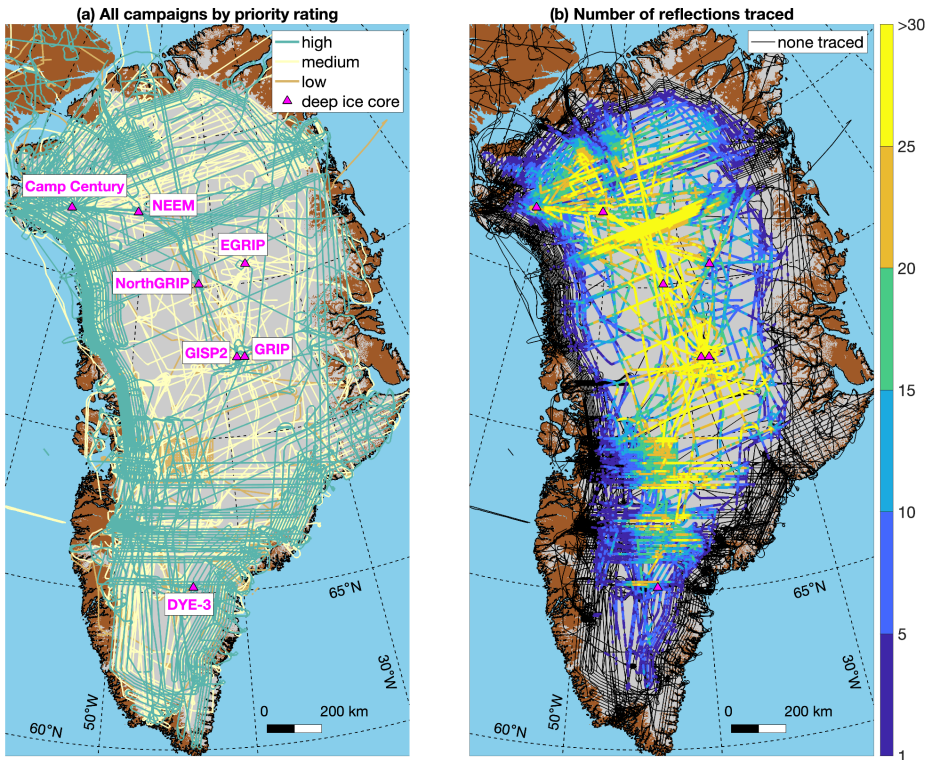
90 ^a See MacGregor et al. (2021) for additional detail on deployed aircraft.

91 ^b Radar sounder nomenclature follows KU/CREStS nomenclature. They maintain a document that details system characteristics for all its
92 surveys before 2010 (https://data.cresis.ku.edu/data/rds/rds_readme.pdf).

93 ^c The qualitative priority rating is described in §2.

94 ^d Total length evaluated includes all segments where the radar sounder was acquiring data, which sometimes includes segments that primarily
95 overflow Arctic sea ice that is not relevant to this study. Gaps within segments are common in earlier campaigns (1993–2001) and complicate
96 length calculations, so here we ignore gaps greater than 10 times the median distance between traces for each segment, leading to generally
97 lower values for those earlier campaigns than reported by M15. Values in parentheses for v1 are campaigns that were not traced by M15
98 because they were either not yet available (2014) or had not been flown at the time (2015–2019). For this study (v2), the total length of the
99 reduced set for each campaign is reported.

100 ^e Number of 1 km segments with at least one reflection traced (same metric as M15). Percentages are of the portion of the dataset evaluated,
101 which differs between M15 and this study.



103

104 **Figure 1:** Airborne radar-sounding surveys collected across the GRIS by KU/CReSIS between 1993 and 2019. Segments are color-coded by
 105 (a) priority rating and (b) maximum number of reflections traced within 1 km segments along-track. Ice, land, and ocean masks are from
 106 Howat et al. (2014) via BedMachine v5 (Morlighem et al., 2022).

107 The two-way traveltimes of both the air–ice and ice–bed reflections have already been traced and recorded in these data
 108 by semi-automated algorithms and quality-controlled (*QC'd*) by KU/CReSIS personnel; the difference between these
 109 traveltimes has been used extensively by others to map ice thickness across Greenland (e.g., Morlighem et al., 2017, 2022).
 110 The ice–bed reflection is harder to trace confidently than the air–ice reflection, and during our examination of the dataset we
 111 occasionally observed possible errors in the former. However, because we are primarily interested in reflection depths, we
 112 only adjusted the air–ice reflection traveltime to address minor but obvious errors that we observed in a very small portion of

113 the dataset that we evaluated (<0.1%). As for M15, when converting two-way traveltime t to depth, we assume that the radio-
114 frequency real part of the relative permittivity of ice is 3.15, equivalent to a one-way radio-wave speed in ice of $168.9 \text{ m } \mu\text{s}^{-1}$.

115 A fundamental difference between M15 and this study revolves around the handling of “repeat-track” flights. This
116 difference arises from the recognition that the lead priority for most NASA airborne surveys of the GrIS by OIB and its
117 predecessors was detecting elevation change of the surface of the GrIS using laser altimetry along the same flight tracks
118 repeatedly (e.g., Krabill et al., 2000; Csatho et al., 2014). In other words, many NASA flights that collected high-quality VHF
119 radar-sounder data across the GrIS did so along a track that was nearly identical to another flight that did the same. M15
120 ignored this issue and evaluated all 1993–2013 data, which complicated subsequent reconciliation of traced reflections into an
121 ice-sheet-wide radiostratigraphy. ~~For example, minor variations in flight track can lead to numerous intersections of two~~
122 ~~slightly different flights, which increases the potential for incorrect matches, and having numerous closely spaced reflections~~
123 ~~can bias subsequent 2-D gridding at the ice-sheet scale.~~ In this study, we explicitly avoid tracing repeat tracks by first collating
124 what we term the *reduced set*. To collate this reduced set, we first assign each campaign a priority rating (Table 1), i.e., an *a*
125 *priori* qualitative assessment of the campaign’s overall radar data quality intended to guide prioritization for further tracing.
126 This rating was mostly based on the radar system used and known campaign outcomes, but we recognize that individual intra-
127 campaign segment quality can vary significantly due to several factors (e.g., environmental RF noise, data-acquisition
128 interruptions, survey altitude change, GNSS or system-timing errors). We then manually inspected a map of the GrIS showing
129 all radar flight tracks and identified all contiguous sets of frames required to “complete” a GrIS radiostratigraphy from the
130 1993–2019 KU/CReSIS data. If any portion of a track was repeated, then only a portion from the campaign with the highest
131 available priority rating was included. While this approach means that many previously traced segments from v1 of the GrIS
132 radiostratigraphy have been effectively discarded, it minimized the work required to review those data. As a result, M15 traced
133 at least one reflection in ~33% of the total dataset it examined, while this study more than doubled that ratio (69%; Table 1).
134 Table 2 summarizes this step and all other major methodological differences between M15 and this study.

135
136 **Table 2:** Summary of key differences between the development of v1 (M15) and v2 (this study) GrIS radiostratigraphy datasets.

Element	v1 (M15)	v2 (this study)
Data selection	All frames from 1993–2013 were investigated.	Campaigns were initially prioritized (Table 1) and then the “reduced set” of non-overlapping frames from 1993–2019 was identified manually based on geolocation and visual assessment of segment quality. Only this reduced set was investigated.
Data pre-processing	Individual frames were reconstituted into ~50 km-long radargrams (“blocks”) with ~1 km overlap on both ends for automated matching of reflections between them.	Individual frames were concatenated, regardless of length, and any pre-existing overlap between them (non-unique traces) was removed.
Reflection prediction	If complex radargrams were available, then phase-tracking was used; if not, then image processing	Only ARESELP was used to predict reflections and only for previously untraced segments from 2014–2019.

Deleted: due to, e.g.,

Deleted: that

Deleted: with each other

	(ARESP) was used, with the option for manual reflection prediction if both those methods failed.	
Radargram visualization	Original (two-way traveltime), free-air-removed (“depth”) or reflection-flattened radargram views available.	Additional thickness-normalized view available where both ice–surface and ice–bed reflections were already traced.
Reflection selection	As many contiguous reflections as observed were selected to be traced.	Distinct and isolated reflections from the upper 80% of the ice column were prioritized for tracing, as these were assumed to be isochronal.
Reflection tracing	Semi-automatic peak following or manual tracing was used, with no cutoff length for the traced reflection.	Semi-automatic peak following was used, with an adjustable cutoff length (typically 10–100 km) to limit erroneous excursions and an automatic stop upon intersection with an existing traced reflection.
Reflection flattening	Either predicted or traced reflections could be used to flatten the radargram for QC and further tracing.	The flattening algorithm was adjusted to consider traced length (indicative of overall quality) rather than just the maximum number of traced reflections to identify the reference location, and it was improved to iteratively predict the depth of reflections not observed at the reference location (where they overlapped with other reflections that did).
Reflection tracing QC	Once all blocks for a given segment were traced, they were merged and displayed in a separate graphical user interface (GUI) for QC.	No additional merging was necessary; after any reflection was traced or adjusted, the GUI required that the sign of the depth difference between each reflection pair be the same throughout the radargram, i.e., that all reflections be stratigraphically conformable with respect to each other.
Reflection matching	Reflections were matched manually using a combination 2-D/3-D GUI, which were then QC’d using network graphs to check for reflection overlap.	Reflections were initially matched automatically based on their depths and the range resolution of the segment’s radar system; these matches were then manually QC’d and supplemented using a 2-D-only GUI.
Firm correction	None applied but a 10 m uncertainty in reflection depth was assumed.	For each trace, the modeled firm air content closest to the acquisition date was used to estimate the firm correction, and the assumed reflection depth uncertainty was reduced to 5 m.
Reflection dating	All six available deep ice cores were used to date reflections that intersected those cores; reflections that were matched to those core-intersecting reflections were dated, and the ages of remaining undated reflections were vertically interpolated where possible.	No major changes, except for the addition of EastGRIP ice core.
Reflection gridding	Normalized isochrone depths were gridded using ordinary kriging onto a 1 km grid.	Similar gridding method but using absolute isochrone depths and onto a 5 km grid, then smoothed.

140

141

142

143

144

145

To ensure the continuity of traced reflections within individual segments and reduce the computing resources required, M15 reconfigured individual radar data frames so that they partly overlapped with each other (typically by ~1 km). However, this process often created more challenges than it solved. In the intervening decade since that study, available computing resources have grown substantially but the data volume of any given SAR-processed segment from the radar systems deployed has remained the same. Here we simply concatenate contiguous sets of frames ([portions of segments](#)) as needed for the reduced

146 set, removing any non-unique traces that are present (whether in time or space). This procedure resulted in 536 sets of
147 concatenated radar data frames that range between 12–3774 km long, with a median length of 250 km. We ultimately traced
148 at least one reflection in 496 (93%) of those concatenated sets ([Fig. 2a](#)).

149 **3 Reflection analysis methods**

150 In this section, we describe the methods we used to trace GrIS radiostratigraphy, QC and date the dataset, focusing primarily
151 on the key differences between this study and M15, all of which were made with the intent of accelerating product development
152 and decreasing uncertainty therein. Table 2 summarizes those key differences in our methodology for pre-processing,
153 predicting, tracing, QC'ing, dating and gridding GrIS radiostratigraphy. Fig. 2 shows the key elements of this workflow.

154

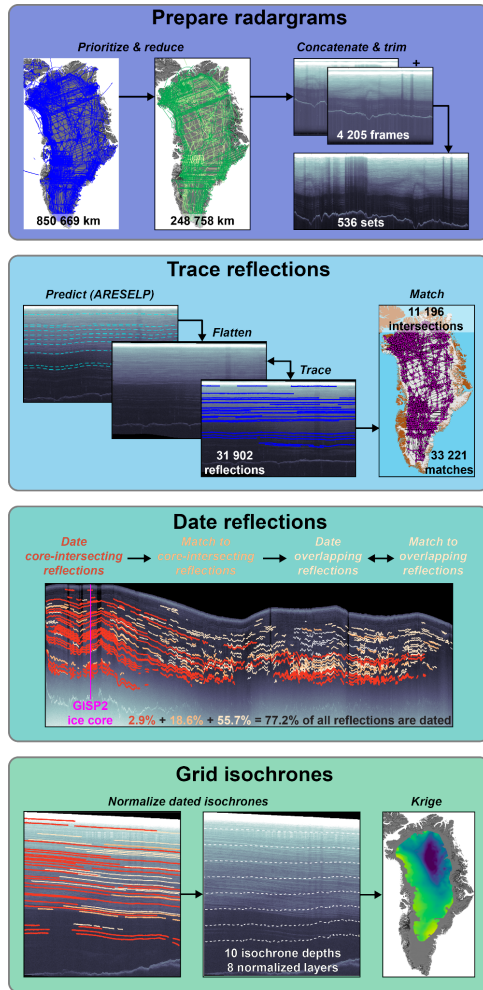


Figure 2: Flowchart illustrating the key steps involved in generating GrIS radiostratigraphy v2. Values given relate to the entire dataset, not just the radargrams shown. (a) Radargram preparation, including selection of the reduced set and concatenation (§2). (b) Typical tracing workflow and subsequent inter-segment reflection matching (§3.1, 3.2). (c) Reflection dating begins at ice cores, is sequentially propagated outward using reflections matched core-intersecting ones, and then any remaining reflections that horizontally overlap with already-dated ones are then dated where possible. The latter two steps are then repeated until no new reflections are dated. White reflections are undated

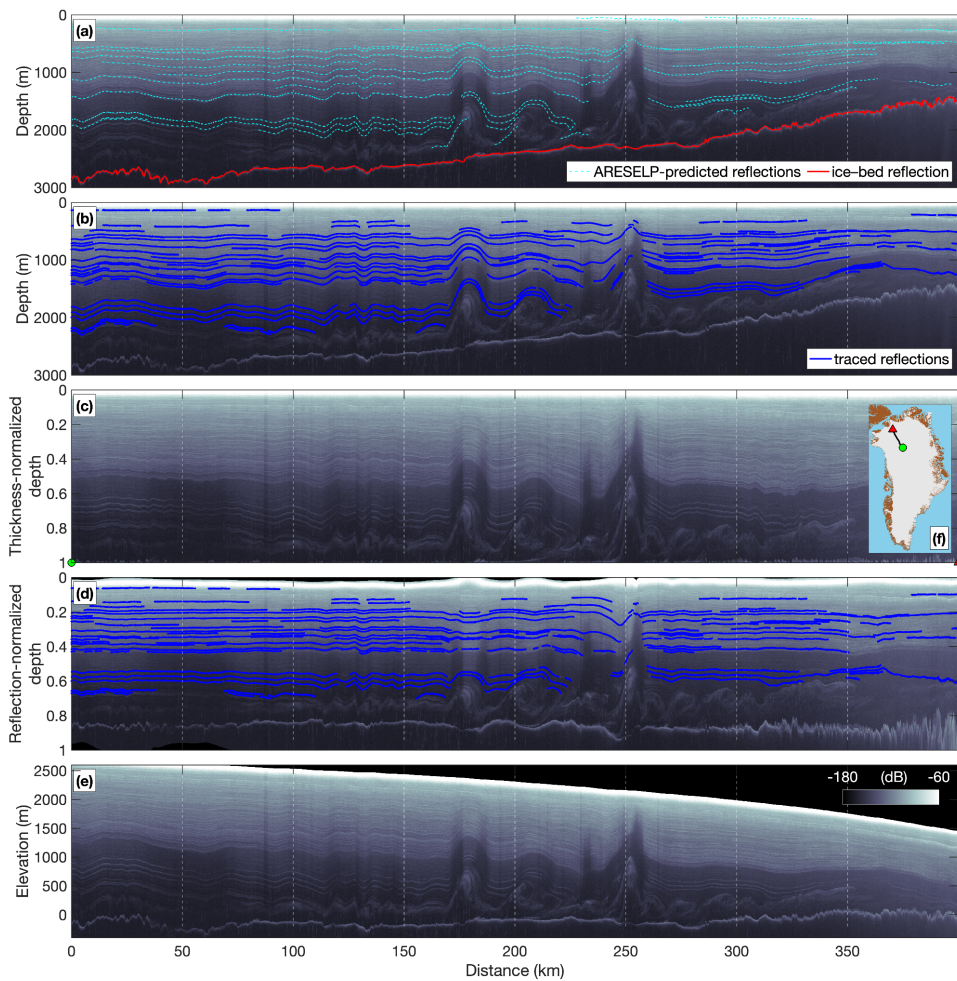
161 [\(§3.3\) \(d\). Gridding isochrones begins by vertically interpolating the dated radiostratigraphy to pre-selected ages/depths, and then each of](#)
162 [those ages/depths are gridded two-dimensionally using ordinary kriging \(§3.3\).](#)

164 3.1 Tracing workflow

165 It is much simpler to confidently trace any reflection if a prediction of its location can be generated automatically beforehand.
166 M15 introduced two automatic methods that leveraged the phase change of the recorded complex signal to predict the slope
167 of internal reflections and – by integrating these slopes along-track – the shape of the reflections themselves. However, these
168 methods were limited by the availability of large-volume, single-channel complex data from KU/CReSIS, and they cannot be
169 applied to data that has already been SAR-focused. In cases where complex data were not available (i.e., most of the 1993–
170 2013 dataset), Automated Radio Echo Sounding Processing (ARESP) was applied, using a refactored version of the ARES
171 algorithm introduced by Sime et al. (2011). However, all three methods focus on estimating reflection slope, as do similar
172 methods introduced later (e.g., Holschuh et al., 2017). As a result, it is often difficult to determine where to automatically
173 terminate a given reflection prediction in a manner comparable to that which often occurs with observed reflections, e.g., they
174 fade out or merge with another reflection. This challenge tends to limit the use of slope-prediction methods to well-behaved
175 radargrams with stable and relatively high signal-to-noise ratios.

176 Alternatively, Xiong et al. (2018) introduced an alternative method that they termed the Automated RES Englacial Layer-
177 tracing Package (ARESELP). This method first identifies candidate reflection peaks vertically using wavelet transforms, prior
178 to then propagating these candidate reflection peaks horizontally using Hough transforms for slope prediction. ~~We selected~~
179 ~~this method for reflection prediction in previously untraced campaigns (2014–2019):~~ ~~1. It does not require complex data; 2. It~~
180 ~~permits reflections to terminate; 3. It often generates realistic synthetic radiostratigraphy; and 4. The algorithm was publicly~~
181 ~~archived.~~ We refactored the ARESELP algorithm (written in MATLAB™) to both accelerate it and improve QC of its output;
182 we then applied it to the 2014–2019 campaigns (Figs. 2b, 3a). Despite our improvements, ARESELP is only used to predict
183 reflection geometry and not as a substitute for tracing itself, as its output quality is variable (Jebeli et al., 2023). For example,
184 ARESELP often identifies the multiple of the air–ice reflection as a candidate internal reflection. Where ARESELP is
185 successful, its outputs were used only to initially “flatten” the radar data (described below) and then discarded, so that no
186 ARESELP-predicted reflections were mistaken for operator-traced ones.

Deleted: Because their method does not require complex data, permits reflections to terminate, often generates realistic synthetic radiostratigraphy and was publicly archived, w...



192

193 **Figure 3:** Multiple visualizations of a portion of a single segment (8 concatenated frames) from 2017-04-13 (20170413_01_049-056) that
 194 approximately follows ice flow from a central ice divide toward the outlet of Petermann Glacier. All radargrams shown at the same color
 195 scale. (a) Untraced radargram in terms of depth, i.e., the variable-length portion of the radargram before the air-ice reflection has been
 196 removed, with ARESELP-predicted reflections overlain. (b) Same as (a) but with traced reflections overlain. (c) Thickness-normalized
 197 radargram. (d) Reflection-flattened radargram. (e) Elevation-corrected radargram (relative to geoid). (f) Location of radargram in Greenland.

198 As illustrated by M15, flattening radar data with respect to predicted or already-traced reflections is both a valuable QC
199 method and one which can accelerate further tracing (Figs. 2b, 3d). Here we continue to use this method with minor adjustments
200 that permit it to more reliably and iteratively estimate the vertical position of reflections that were not observed at the reference
201 location but which overlap with ones that were. However advantageous, this flattening method requires that either predicted
202 or traced reflections are already available, which is not always the case. Inspired by earlier studies concerned with the physical
203 interpretation of radiostratigraphy and modeling thereof, especially Nereson et al. (1998) and Hindmarsh et al. (2006), here
204 we introduce an additional radargram reprojection that is *thickness-normalized*, which requires only that the air–ice and ice–
205 bed reflections already be traced, as is the case for nearly all the KU/CRISIS dataset we evaluated. Normalization by ice
206 thickness is commonly applied in analytic and numerical models of ice flow to ease interpretation, but to the best of our
207 knowledge it has not been applied previously to the returned power P_r displayed in radargrams themselves, even though it can
208 accelerate tracing. In the nomenclature of Hindmarsh et al. (2006), thickness normalization of radargrams also offers a rapid
209 way of evaluating whether internal reflections drape over subglacial topography (i.e., they are essentially a shallower and
210 smoother version of the ice–bed reflection) or override it (i.e., variations in reflection depth bear little resemblance to the ice–
211 bed reflection and are mostly negligible). Following thickness normalization, draping reflections should be flatter, while
212 overriding ones could be rougher. In practice, because relatively few of the flight tracks considered here both follow present
213 ice flow *and* contain interpretable radiostratigraphy (Sime et al., 2014; Cooper et al., 2019), such a straightforward
214 glaciological evaluation (draping vs. overriding) is often difficult. We note that alternative physically based vertical
215 reprojections of radar data are conceivable, such as the coordinate transform for ice-flow models described by Parrenin et al.
216 (2006), but here we focus on the simplest to implement and interpret for reflection tracing.

217 To perform this thickness normalization, the surface and bed traveltimes, $t_s(x)$ and $t_b(x)$, respectively, are first smoothed
218 using a 3-km-long locally weighted filter in the along-track direction x . The normalized depth coordinate z is
219 $(t - t_s(x))/(t_b(x) - t_s(x))$. Because $t_s(x)$ and $t_b(x)$ both vary along-track, the number of fast-time samples that form the
220 radargram between them also varies, so the vertical interval between samples $\Delta z = z_{i+1} - z_i$ also varies along-track. The
221 thickness normalization is a vertical rescaling that does not directly alter the returned power $P(x, t)$ that constitutes the
222 radargram, so if the vertical resolution of the displayed radargram can also vary along-track, then the thickness-normalized
223 returned power $P(x, z)$ can be displayed with no change in amplitude from $P(x, t)$. In practice, it is simpler and more
224 computationally efficient to display two-dimensional (2- D) matrices with two monotonic axes. Thus, the second and final step
225 is to vertically interpolate $P(x, t)$ onto a single monotonic z vector that has the same number of samples as the original
226 radargram and ranges from 0 to 1, which sometimes slightly degrades the signal-to-noise ratio of $P(x, z)$ relative to $P(x, t)$.
227 As for reflection-based flattening, reflection traveltimes can be similarly vertically reprojected, or traced within this projection
228 and then reprojected to the radargram’s original vertical frame of reference (t). This reprojection is simpler than that for
229 reflection-based flattening, is also parallelizable, and it is particularly valuable for initial reflection tracing within radargrams
230 where $H(x)$ varies substantially, as it reduces the need to adjust the vertical axis when tracing.

231 In terms of selecting which reflections to trace, for v2 we focused exclusively on those that we deemed most likely to be
232 isochronal. Specifically, we focused on distinct, relatively isolated reflections in the upper ~80% of the ice column that are
233 observed across many radargrams, are not diffuse (i.e., difficult to trace using semi-automatic peak following), and do not
234 form part of a disrupted basal unit. While the above criteria represent an effort to ensure the validity of a core assumption of
235 our approach (reflection isochroneity), we are not aware of direct observations of unconformable reflections that are both
236 within the GrIS interior and above disrupted basal units that contradict this assumption, as have been observed in Antarctica
237 (e.g., Das et al., 2013). Deeper basal ice in the GrIS interior and strata exposed at the ice margin can clearly be disrupted,
238 overturned and probably unconformable (Dahl-Jensen et al., 2013; MacGregor et al., 2015a, 2020; Panton and Karlsson, 2015;
239 Bons et al., 2016; Leysinger-Vieli et al., 2018), so we mostly avoid tracing reflections within this zone unless they meet other
240 criteria and are identifiable across a large distance or several radargrams. As a result, several deeper reflections mapped by
241 M15, which were typically the top of disrupted basal units, were removed during our review of the v1 dataset.

242 We continue to use semi-automatic peak following to trace reflections, typically using a very narrow fast-time (vertical)
243 sampling window (± 1 sample; 1.7–5.3 ns, equivalent to 1.4–4.5 m, depending on campaign) between traces, but sometimes
244 ± 2 samples and rarely ± 3 samples for especially steep reflections. The algorithmic speed of this method outweighs its relative
245 simplicity, as it permits faster tracing *and* faster correction of inevitable errors therein. To limit these errors, we terminate
246 propagation of a candidate reflection automatically once another existing reflection is intersected or where tracing has
247 propagated a prescribed distance limit from the manually selected inception (typically 25–100 km, depending on radargram
248 quality and reflection slope) – whichever is first.

249 A critical addition to the tracing workflow relative to M15 is an algorithmic check for
250 stratigraphic conformability following the tracing of any reflection or modification
251 thereof. This QC check simply requires that the sign (either >0 or <0) of the depth
252 difference between any pair of reflections be both non-zero and the same throughout the
253 radargram. In other words, no traced reflection can be both above and below another. This
254 check automatically identified occasional tracing errors in the v1 radiostratigraphy that
255 we rectified, and it simplified the process of QC'ing v2. Once tracing is complete, all
256 reflections were vertically re-adjusted by $\leq \pm 1$ fast-time (vertical) sample to match the
257 local maximum in P_r . This adjustment also increases the value of recorded reflection P_r values for future investigations
258 (e.g., MacGregor et al., 2015b).

259 3.2 Inter-segment matching

260 Once tracing was complete, intersections between traced segments were identified automatically, with an algorithm that
261 requires a minimum intersection angle of 5° between segments in map view and limits identified intersections to a maximum
262 along-track density of 5 km within any given segment. The combination of the reduced set and these intersection selection

263 criteria generated 24% fewer intersections than v1 (11 196 vs. 15 148), which simplifies subsequent reflection matching (Fig
264 2b). Assuming a uniform reflection matching error rate, fewer matching errors will be made if there are fewer intersections to
265 evaluate.

266 Matching reflections between traced segments and between distinct radar systems is a significant challenge for large
267 radiostratigraphic datasets. While M15 evaluated automatic matching, they ultimately did not use it. Here we generate an initial
268 set of reflection matches automatically, with an algorithm that limits inter-segment matches to those with a mean depth
269 difference no more than three times the maximum range resolution of the segment pair's radar system (2.4–4.4 m for most
270 systems considered) within 500 m of their intersection. These automatic matches were then QC'd using network graphs to
271 verify stratigraphic conformability between reflection pairs, using an algorithm similar to that applied when tracing individual
272 segments (§3.1), i.e., if a segment contains two reflection that overlap horizontally, then they cannot both be matched to the
273 same reflection in another segment. Additional matches were then identified manually, which were then again QC'd using
274 network graphs. In M15, matches were not permitted between the earliest campaigns (1993–1997) and later ones due to their
275 difference in range resolution; here we permit such matches as prominent traced reflections were often similar across all
276 campaigns.

277 3.3 Dating and gridding

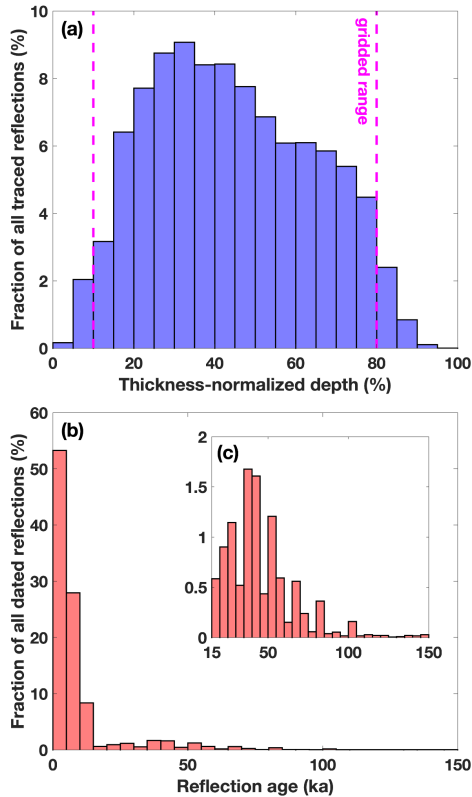
278 Once traced, matched and merged, reflections must be dated to be of maximum value to the broader scientific community.
279 Our dating algorithm is mostly unchanged from M15, to which we refer the reader for further details. We are unaware of any
280 substantive improvement in reflection dating methodology developed since then, although alternatives exist if better estimates
281 of accumulation histories or modern dielectric profiling ice-core data are available (Cavitte et al., 2021; Franke et al., 2025).
282 To date traced radar reflections across an ice sheet, multiple dated and synchronized ice cores are required. We use the same
283 six deep ice-core depth–age scales as M15 (their Table 2), but supplement them here with the addition of the partially complete
284 EastGRIP (*EGRIP*) depth–age scale from Mojtabavi et al. (2020). This depth–age scale includes the upper 1884 m of the ice
285 column – approximately three quarters thereof given an ice thickness of ~2550 m – which records the period 0–15 ka.
286 Compared to M15, we slightly relax the search radius within which a radar segment is considered to have “intersected” an ice
287 core from 3 to 5 km, increasing the number of core intersections from 53 to 65. The use of the reduced set (no repeat tracks)
288 also decreases dependence on the Camp Century ice core, which was overrepresented in the v1 dataset (47% of all intersections,
289 as compared to 31% in this study). We continue to use the “quasi-Nye” dating method introduced by M15 to vertically
290 interpolate the age of undated reflections that are either sandwiched between or are vertically near pairs of dated reflections
291 (no more than the thickness of a dated layer pair or 20% of the ice thickness, whichever is less). This method seeks the best-
292 fit vertical strain rate that can match the depth–age relationship of the two bounding reflections, and then uses this vertical
293 strain to interpolate the age of the undated reflection – or extrapolate where appropriate (Fig. 2c).

294 Previously, an undated reflection could only be dated if it did not cause the vertical profile of age anywhere in the segment
295 to decrease with depth. Here we relax this requirement slightly to accommodate potential matches of vertically closely spaced

Deleted: in review

297 reflections by instead requiring that the age of the putative dated reflection be within 5% of the uncertainty in age of adjacent
298 dated reflections. This relaxation accommodates slight mismatches in age between reflections that intersect different ice cores.
299 Finally, where sufficient dated reflections exist, we use quasi-Nye interpolation to estimate the along-track depth of a set of
300 “synthetic” isochrones at predetermined ages. We include the same set of five ages generated by M15 (9, 11.7, 29, 57 and 115
301 ka) along with five more of additional paleoclimatic interest [from the Late and Early Holocene, the bounds of the Bolling-
302 Allerød period during the Last Glacial Period, and an approximate Last Glacial Maximum](#) (3, 8, 12.8, 14.7, and 19 ka;
303 [Rasmussen and others, 2006](#)).

304 Similar to M15, we use ordinary kriging to grid the depths of the 1-D along-track
305 isochrones onto a 2-D grid using the Python geostatistical simulation software package
306 GStatSim (v1.0.6; MacKie et al., 2023). We also use quasi-Nye interpolation (M15) to infer
307 the age at predetermined thickness-normalized depth intervals along all traced segments
308 and then grid these ages as well. We select a 5 km grid in the standard EPSG:3413 projection
309 – rather than 1 km as in M15 – to focus on the large-scale age structure of the ice sheet.
310 Contrary to M15, we find that absolute depths are smoother at large scale than thickness-
311 normalized depths, so we grid the former instead. We find that a zero-nugget spherical
312 semivariogram model is a better representation of the experimental semivariogram of
313 shallower/younger isochrones (≤ 19 ka), while an exponential model is better suited to
314 deeper/older ones. For the age at regular depth intervals, we restrict the gridding to the
315 middle 70% of the ice column (10–80% ice thickness) at 10% intervals as this depth range
316 captures the range of most traced reflections (Figs. 2d, 4); we find that spherical variograms are most
317 suitable at all depths. This normalized depth range is more conservative than for M15 (4–100% ice thickness at 4% intervals).
318 Independent variogram models are applied to each depth/age, as opposed to a single variogram model as in M15. We apply a
319 2-D Gaussian smoothing filter to all the resulting grids to reduce noise from individual traced segments and fill in small,
320 enclosed gaps using natural neighbor interpolation. Finally, we blank out any portions of the grid that would result in age
321 overturning (unconformities) relative to other adjacent grids.



323
 324 **Figure 4:** (a) Histogram of the normalized depth of all traced reflections (both dated and undated). Vertical magenta dashed lines highlight
 325 the normalized depth range for which the age of the ice sheet is gridded. (b) Histogram of the age of dated reflections. (c) Zoom-in of panel
 326 b on the pre-Holocene age range.

327 3.4 Depth and age uncertainty estimation

328 The depth uncertainty of the traced reflections is principally attributable to the assumed radio-wave velocity in pure ice
 329 and a correction for spatiotemporally variability firm air content. As for M15, we assume that the real part of the radio-frequency
 330 complex relative permittivity of pure ice ϵ'_{ice} is 3.15, equivalent to a radio-wave velocity in ice v_{ice} of $168.9 \text{ m } \mu\text{s}^{-1}$. M15 did
 331 not directly apply a firm correction and instead attributed a constant and uniform 10 m depth uncertainty to all traced reflections.
 332 Since then, substantial progress has been made in the modeling and validation of the firm air content in the near-surface of ice

333 sheets, due to its importance for interpretation of satellite altimetry data (e.g., Medley et al., 2022). The total firn air content is
334 equivalent to the firn correction that is commonly applied to radar-sounding data to correct reflection depths. Here we use the
335 modeled firn air content developed by Medley et al. (2022) for the period 1980–2021 across Greenland and Antarctica to
336 determine the local firn correction for each radar trace from the nearest 5-d simulation interval to the acquisition date. We then
337 assume that the reflection depth uncertainty associated with the firn correction is reduced to 5 m. The median modeled firn
338 correction applied is ~19 m, but it can be up to ~25 m.

339 The age uncertainty for each dated reflection is calculated following the same methods described in further detail by M15.
340 For core-dated reflections, this total age uncertainty is the combination of the reported uncertainties in the ice-core depth–age
341 scales (unchanged from M15), the depth uncertainty of the reflection (discussed above), and the uncertainty induced by the
342 range resolution of the radar system used. The latter quantity depends on the signal-to-noise ratio (SNR) of the reflection at its
343 closest approach to the ice core, which is typically ~5 dB, so for simplicity we assume that quantity is uniform for all core-
344 dated reflections. For reflections dated using quasi-Nye dating, an additional uncertainty is included that accounts for the
345 interpolation/extrapolation of age, which is based on the age uncertainties of the existing dated reflection pair and the variance
346 of the interpolated/extrapolated age across the overlapping section (Equation 12 in M15).

347 To estimate the uncertainty of the 2-D grids, we first also vertically interpolate the along-track depth (age) uncertainty of
348 dated reflections to the age (depth) of interest and then kriging these quantities using the same variogram model parameters as
349 for their respective age (depth) of interest. These kriging-derived uncertainties are then combined with the kriged uncertainty
350 for the parameter of interest (depth or age) as the square root of the sum of squares (M15 only considered the latter term).

351 4 Results

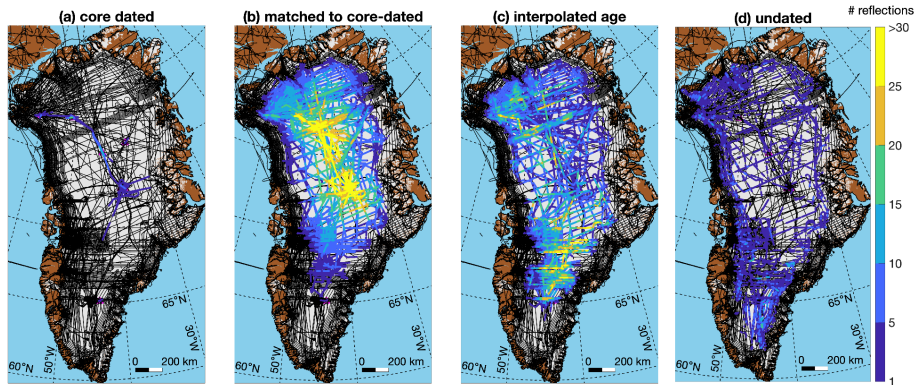
352 The generation of the reduced set, where we downselect repeat flight tracks to a single instance acquired with the highest-
353 fidelity radar system, substantially reduces the number of radargrams that must be examined to generate a complete GrIS
354 radiostratigraphy from NASA/NSF airborne radar-sounding data. For this second version of the radiostratigraphy dataset (v2),
355 we reviewed only 36% of the 1993–2013 radargrams, as compared to 100% for v1. However, we recorded a traced reflection
356 in 65% of the 1993–2013 radargrams examined (112 213 of 172 062 km), as compared to 33% for v1 (160 233 of 482 903
357 km). While we preserved fewer line kilometers of reflections for 1993–2013, we added 58 610 km from 2014–2019 acquired
358 using generally higher-fidelity radar systems.

359 GrIS radiostratigraphy v2 contains 31 902 individual traced reflections of widely varying lengths. Of these reflections,
360 2.9% were dated “directly” where they intersected ice cores, 18.6% by automatically or manually identified matches to those
361 core-dated reflections, and another 55.7% using quasi-Nye dating, leaving 22.8% of traced reflections undated (Fig. 2c). Direct
362 core-dating of reflections is essential but – following our particular tracing strategy – results in a very limited spatial
363 distribution of dated reflections, mostly following the northern part of the central ice divide (Fig. 5). Reflections matched to
364 those core-dated reflections significantly expand the coverage of dated reflections, especially in central and northern

Deleted: OurThis second version of a radiostratigraphic dataset of the ...

Deleted: from NASA/NSF airborne radar-sounding data

368 Greenland. Farther south, where reflections become discontinuous, age interpolation of dated reflections is especially
369 important between ~65–71°N. Undated reflections remain mostly around the periphery of the GrIS, in fast-flowing regions
370 such as Sermeq Kujalleq, and in southern Greenland south of ~68°N.
371

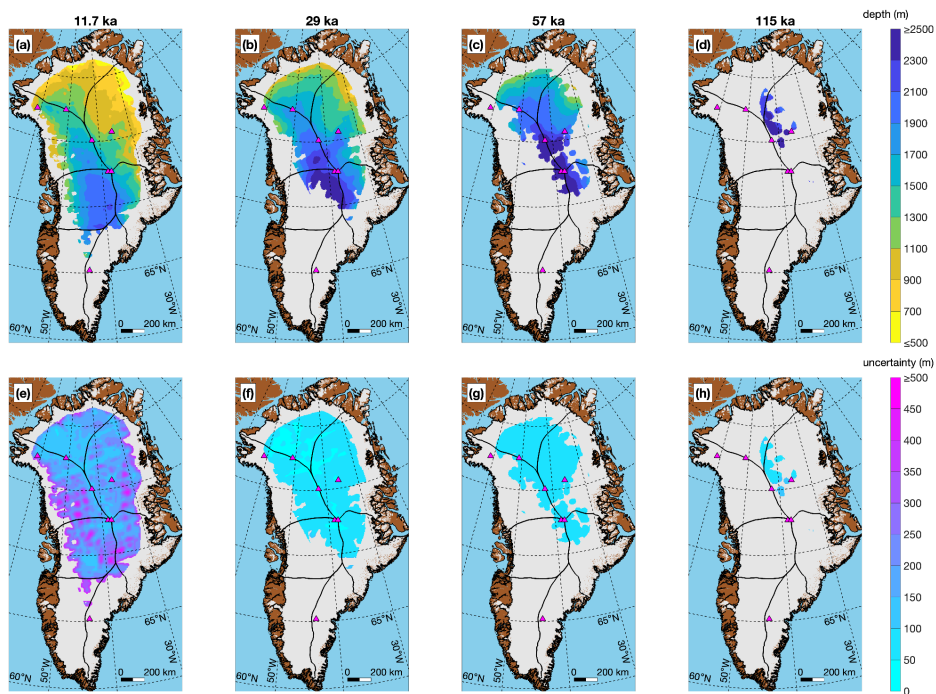


372
373 **Figure 5:** Number of traced reflections by the method in which they were dated.
374

375 For completeness and validation, we generated Movie S1, which shows all traced segments in an elevation-corrected
376 reference frame. This movie illustrates both the breadth of the traced reflections and the considerable number of *un*traced
377 reflections, which are typically discontinuous and less distinct – but not exclusively so. Most (94%) reflections were traced in
378 a depth range within 10–80% of the ice thickness, following both our stated prioritization, signal loss with increasing depth,
379 and the challenge of tracing distinct very shallow reflections within most of the KU/CReSIS dataset that we evaluated. The
380 large majority (86%) of all dated reflections are from the Holocene (11.7–0 ka; Fig. 3b), which is consistent with previously
381 observed patterns of radar reflectivity across the ice sheet. Some of the most distinct reflections are from the Last Glacial
382 Period (115–11.7 ka), in particular the well-known trio observed throughout northern Greenland (37.7, 44.7 and 50.7 ka,
383 respectively), so they are also often some of the most contiguous or readily matched between segments so they tend to be
384 under-represented in the distribution of all dated reflections compared to numerous and sometimes difficult-to-match shallower
385 Holocene reflections.

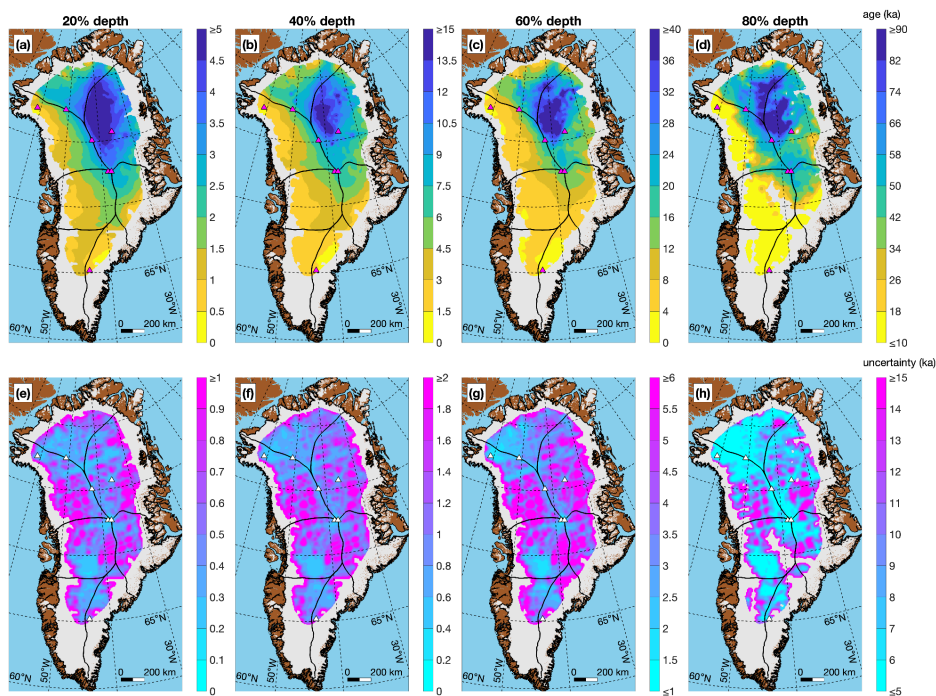
Deleted: –11.7

Deleted: –115



388 **Figure 6:** (a–d) Gridded depth of four out of the ten gridded synthetic isochrones (11.7, 29, 57 and 115 ka, respectively). (e–h) Gridded
 389 uncertainty in these isochrones. Ice drainage basins (black lines) are from Mougintot et al. (2019).
 390

391 The resulting depth/age grids cover up to 65% of the ice sheet by area (Figs. 6 and 7). The uncertainties in the resulting
 392 datasets also are slightly more completely expressed than by M15. In comparison to similar depth/age grids produced by M15,
 393 it is clear that producing a dated GrIS radiostratigraphy within ~100 km of the ice margin or south of ~68°N remains
 394 challenging. Neither version of the dataset does so consistently, except for v1 along parts of the northern margin of the GrIS,
 395 which we attribute to less conservative kriging parameters than those applied in this study. We attribute this broader challenge
 396 not to the sparsity of surveys (Fig. 1) but rather to the absence of traceable radiostratigraphy (less common) or the low
 397 continuity of observed radiostratigraphy (more common), which makes it less feasible to trace efficiently using this study's
 398 methods and was not prioritized (Movie S1). This result is consistent with earlier automated assessments of radiostratigraphic
 399 continuity by Sime et al. (2014) and M15, particularly in terms of where traceable radiostratigraphy is present (although not
 400 necessarily dateable).



401 **Figure 7:** (a–d) Gridded age of four out of the seven gridded ages at 20, 40, 60 and 80% of ice thickness, respectively. (e–h) Gridded
 402 uncertainty in these ages. Note each panel has a different color scale, whereas for each row of Fig. 6 the color scale is the same.
 403

404 As observed by M15 and reproduced here, the oldest ice at most depths is observed in the southeastern portion of the
 405 northernmost ice drainage basin and the northwestern portion of the northeastern drainage basin (northwest of the Northeast
 406 Greenland Ice Stream). Any potentially conformable Eemian ice (130–115 ka) is likely also located there (Fig. 6d). These
 407 results are qualitatively consistent with observations of outcropping pre-Holocene along the northern margin of the GrIS
 408 (MacGregor et al., 2020). Any substantial (>100 m) conformable layer of pre-Holocene basal ice is likely absent south of
 409 ~65°N, which is consistent with the higher long-term accumulation rates there (e.g., MacGregor et al., 2016a).

410 The gridded uncertainty of the synthetic isochrones (Fig. 6e–h) varies significantly and does not necessarily increase with
 411 depth. Assuming comparable relative uncertainties for all dated reflections, it also depends on proximity (in age) of the
 412 synthetic isochrone to dated reflections. While reflections were regularly traced near the onsets and terminations of the Bølling-
 413 Allerød period (14.7–12.8 ka), the Younger Dryas cold period (12.8–11.7 ka) and the Holocene epoch (11.7 ka–present), much
 414 more common are yet younger reflections (Fig. 4a) from which the depth of those onsets/terminations were sometimes

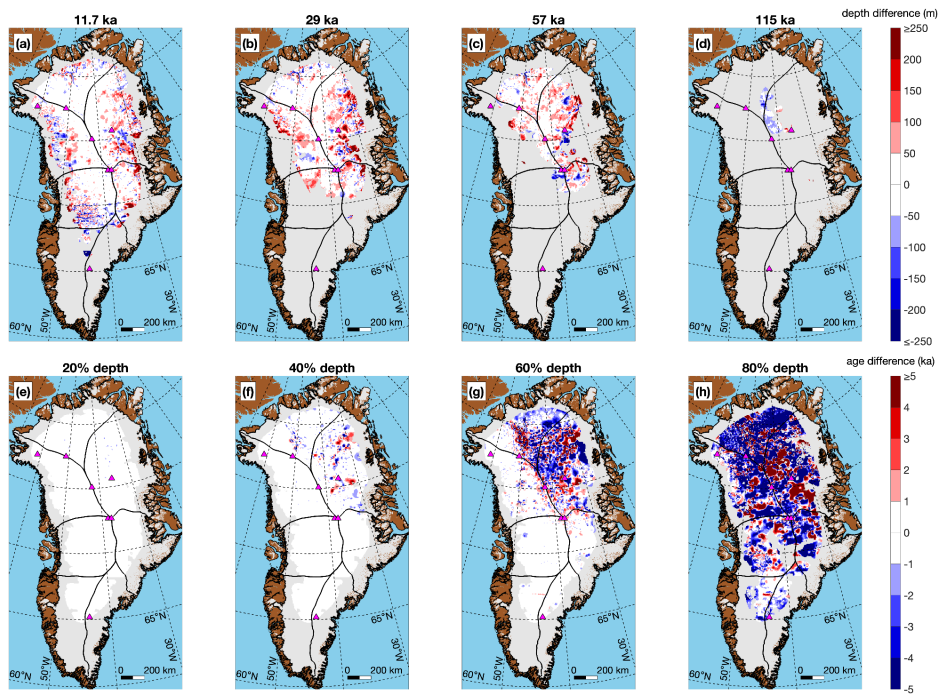
Deleted: -130

416 estimated. In contrast, the prominent trio of older reflections mentioned above that are often observed together in the northern
417 GrIS represent a more spatially limited but stronger constraint on the location of some older climate transitions (e.g., Fig. 4f,g).

418 This study's gridded fields are generally similar to those in M15 (Fig. 8). We attribute most differences to improved
419 coverage and QC in this study, the more conservative coarser grid resolution (5 km vs. 1 km) and the final smoothing applied.
420 For the isochrone depths, as expected the differences increase toward the ice margin and away from ice core sites with a slight
421 trend toward increasing magnitude with increasing isochrone age. The gridded age differences display a more complex spatial
422 pattern. Their differences are lower at shallower depths, as expected, but increase significantly at 60% depth particularly in the
423 older northern and northeastern drainage basins. At 80% depth – the maximum normalized depth we considered – the
424 magnitude of the differences is large but varies in sign, with an increasing magnitude trend toward the north.

425 Franke et al. (2023) presented multiple gridded isochronal datasets for the northern GrIS from OIB and other campaigns
426 led by the Alfred Wegener Institute (*AWI*), which could be compared to our gridded products. However, because they gridded
427 directly traced isochrones, rather than the synthetic isochrones at climate transitions that we focused on, based on the ages of
428 their isochrones alone most of our gridded isochrones are not directly comparable with theirs. Only one is potentially
429 comparable with our 11.7 ka isochrone (Fig. 8a), which is their 12.0 ka isochrone for the Petermann Glacier onset region.
430 However, given the two-order-of-magnitude difference in grid resolution between their isochrone (0.05 km) and ours (5 km),
431 along with the smoothing we applied, we do not consider such a comparison meaningful.

432



433

434 **Figure 8:** (a–d) Difference in gridded depth of four isochrones mapped by this study from M15. (e–h) Same as above, except for the age at
 435 normalized depths.

436

5 Discussion

437

438

439

440

441

442

443

444

Much has been written about the potential value of – and the challenge of producing – large-scale ice-sheet radiostratigraphy datasets (e.g., Karlsson et al., 2013; Sime et al., 2014; Moqadam and Eisen, in review; Bingham et al., in review). As with all methods of observation or data analysis, future improvements therein are almost inevitable. However, at some point the unique capabilities of the system in question – whether they be resolution, speed, accuracy or some other characteristic – must be locked so that the observation or analysis of interest can be made. Both M15 and this study assessed several methods for accelerating tracing but – critically – eventually paused that assessment and shifted gears to the actual production of an ice-sheet radiostratigraphy. This production stage revealed several challenges associated with QC’ing, dating and normalizing a large-scale radiostratigraphy (e.g., Fig. 2; §3), but several subsequent related studies have focused mostly

445 on designing or assessing alternative methods for tracing or slope estimation (e.g., Panton, 2014; Delf et al., 2020), with
446 relatively few that consider dating reflections not observed at ice cores (Cavitte et al., 2021). Further, it is now well established
447 that it is relatively easy to trace many reflections in any one of the two dozen or so high-quality KU/CreSIS VHF radargrams
448 that cross the northern GrIS (Fig. 1b; e.g., Panton, 2004; Xiong et al., 2018). It is much harder to trace discontinuous reflections
449 within ~300 km of the ice margin, harder still within ~100 km, and even harder to confidently propagate ages from interior ice
450 cores toward the periphery.

451 Despite the clear advantage of scale provided by our approach to mapping radiostratigraphy, our current approach
452 possesses some limitations that could be addressed in future versions. A primary limitation is that – while the GrIS
453 radiostratigraphy v2 dataset depends critically on the spatial relationships between segments and the matches between their
454 traced reflections – it is not a modern relational database through which updates to any individual element propagate
455 automatically. Instead, it is a series of static datasets developed in sequence (concatenated radargram segments, traced
456 reflections, inter-segment reflection matches, reflection ages, and gridded depths/ages). In other words, if an error in tracing
457 any reflection is identified and adjusted, then any matches between that reflection and others must be manually re-verified and
458 the dating and gridding procedures would need to be re-run. A second but more tractable challenge is the dynamic display of
459 intersecting segments and associated traced reflections on 2-D radargrams, which would clarify how far to attempt to trace
460 reflections to maximize the potential for matching them between segments. Alternatively, such inter-segment relationships can
461 sometimes be obvious in three-dimensional (3-D) perspectives of intersecting radargrams and their traced reflections (e.g.,
462 Franke et al., 2023). However, we experimented extensively with such 3-D perspectives in both MATLAB™ and PyVista
463 (Sullivan et al., 2019) and found that modifying or matching mapped radiostratigraphy remains cumbersome in 3-D when
464 evaluating many segment intersections (11 196 in this study).

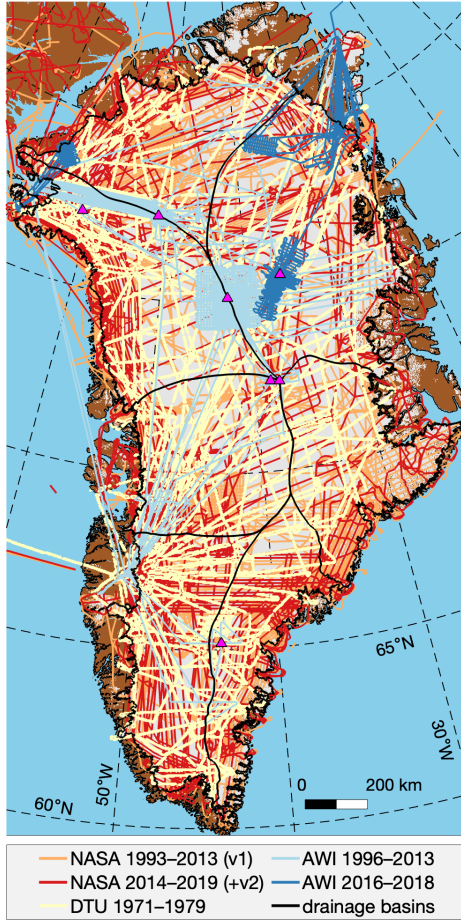
465 To address the challenge of extracting useful geophysical information from large data volumes, machine learning (ML)
466 methods have been increasingly deployed in many fields of Earth science. The constellation of ML methods clearly possesses
467 great potential for accelerating the tracing of radiostratigraphy, but they face several broad challenges before they can be
468 widely adopted (Moqadam and Eisen, in review; Moqadam et al., in review; Peng et al., 2024). First, most ML methods use
469 supervised learning, which typically requires large training datasets. In this case, such datasets would be radargrams that have
470 been traced exhaustively, i.e., those that possess few or no false negatives. However, all presently available large-scale
471 radiostratigraphy datasets – including the one presented in this study – left innumerable observed reflections untraced. These
472 reflections were typically less distinct, less bright or shorter – and so they were deprioritized in our workflow (§3.1). We
473 suggest that suitable ML methods for tracing radiostratigraphy are those that can better tolerate inevitable and copious false
474 negatives, perhaps by being trained on synthetic radargrams or using ARESELP-generated predictions (Culberg and Schroeder,
475 2021; Jebeli et al., 2023). A second and related issue is the question of which reflections should be traced. An answer with a
476 future ML application in mind could simply be “all of them”, but perhaps a more realistic and readily achievable answer is
477 “those that models seek to match”. In the latter more restrained scenario, which was implicit in our tracing strategy, we may
478 consider both which observed reflections are clearly distinct from others *and* those which models seek to reproduce to better

479 resolve ice-sheet history, i.e., typically those associated with or close to major climate transitions (e.g., Born and Robinson,
480 2021; Sutter et al., 2021). However, how to enable ML to perform a similar prioritization remains unclear. Third, as emphasized
481 by Delf et al. (2020) and applicable to all automated methods for tracing radiostratigraphy, improving our ability to automate
482 the matching of reflections across discontinuities – whether due to an acquisition malfunction or observation limitation such
483 as steep reflection slopes – remains an outstanding challenge, and it is not yet clear how ML can accelerate this process.

484 As originally conceived, this dataset (GrIS radiostratigraphy v2) would have included additional VHF airborne radar-
485 sounding data collected primarily by institutions besides the US (Fig. 9). These include the first such data collected across the
486 GrIS during the 1970's by a Danish–British–American consortium that was recently digitized by Karlsson et al. (2024), surveys
487 of the northern and central GrIS mostly from the 1990s led by AWI (e.g., Nixdorf and Göktas, 2001), and more recent AWI
488 surveys using newer CReSIS-built radar systems (e.g., Kjær et al., 2018; Franke et al., 2022, 2023; Jansen et al., 2024).
489 Including these data was ultimately beyond the scope of this study but remains possible and could help fill remaining gaps in
490 coverage – especially in the northern half of the GrIS. A potential challenge in incorporating these data would be their different
491 center frequencies and bandwidths, which result in different patterns of interfering reflections – particularly in reflection-rich
492 Holocene ice. For the newer AWI data (2016–present), this challenge is due to the higher center frequency and wider bandwidth
493 of the system used that would typically result in more reflections being distinguishable, whereas for the other mostly older
494 data the challenge is reversed. Because we found that certain distinct reflections could be matched between KU/CReSIS
495 systems from 1993 all the way through to 2019, there is reason for cautious optimism in merging such disparate datasets.
496 Further, there is precedent in Antarctica for similar multi-system reconciliation of radiostratigraphy (Bodart et al., 2021; Winter
497 et al., 2017; Cavitte et al., 2021; Franke et al., 2025), and the bandwidth of some of the older AWI data (short chirp mode) or
498 the newer AWI data operated in narrowband mode is comparable to most of the radar systems considered here. For the older
499 1970's data, their greater geolocation uncertainty may also present an additional challenge in matching reflections with those
500 from newer systems.
501

Deleted: GrIS

Deleted: in review



504 **Figure 9:** Airborne radar-sounding surveys collected across the GrIS led by various institutions that could be included in future versions of
 506 a GrIS radiostratigraphy (AWI: Franke et al., 2023; O. Eisen and D. Steinhage, pers. comm., 2020; DTU: Karlsson et al., 2024), as compared
 507 to that collected primarily by NASA/KU/CRISIS between 1993–2019.

508 Given its improved spatial coverage, more robust QC and more accessible data formatting (§6), we expect that this second
 509 version of the GrIS-wide radiostratigraphy will help fully realize part of the original purpose for generation of the M15 dataset
 510 – to “[provide] a new constraint on the dynamics and history of the [GrIS]” – but also to expand the range of potential

511 applications for such a dataset. The v2 gridded products can be used to evaluate the modern age structure of initialized ice-
 512 sheet models to validate their overall climate sensitivity and various model parameterizations, especially past accumulation
 513 rates (e.g., Born and Robinson, 2021; Sutter et al., 2021; Rieckh et al., 2024). Following the methods introduced by those
 514 recent studies, the capability to record and advect ice age non-diffusively using a Lagrangian approximation was also
 515 introduced recently (in v2.1) to the widely used Parallel Ice Sheet Model (<https://www.pism.io/>; e.g., Aschwanden et al., 2019),
 516 which expands the potential user base for model evaluation of the age structure of the GrIS. At coarser scales, the gridded
 517 datasets can be more reliably used to distinguish between Holocene and pre-Holocene ice, which is valuable for radiometric
 518 studies of radargrams (e.g., MacGregor et al., 2015b; Chu et al., 2018) and interpretation of bulk rheology (e.g., MacGregor
 519 et al., 2016a). Finally, the along-track traced reflections can be used to rapidly identify anomalous structures within the ice
 520 sheet that can be either diagnosed simply using steady-state models (e.g., MacGregor et al., 2016b) or targeted for more detailed
 521 diagnosis using structural analyses (e.g., Franke et al., 2022).

522 **6 Code and data availability**

523 The MATLAB™ GUIs, functions and scripts and Jupyter notebooks used to perform the analysis and generate the figures in
 524 this manuscript are available at <https://doi.org/10.5281/zenodo.14183061> (MacGregor, 2024a). Most of the analysis was
 525 performed using functions built-in to several versions of MATLAB™ (R2022a to R2024b) with its associated Image
 526 Processing, Mapping, Statistics and Wavelet toolboxes. Python v3.12, various standard packages, and GStatSim were used to
 527 krig the dataset (MacKie et al., 2023).

528 The datasets resulting from this study, which together constitute version 2 of Greenland’s deep radiostratigraphy, are
 529 available at <https://doi.org/10.5281/zenodo.15132763> (MacGregor et al., 2025) and may also be later made available through
 530 the National Snow and Ice Data Center, where further dataset-specific documentation will be provided. Table 3 describes the
 531 format of the HDF-5-compatible MATLAB™ (v7.3 .mat) files that contain each campaign’s traced reflections for each
 532 segment. Table 4 describes the format of the GeoPackage (.gpkg) files that contain the depths of each segment’s traced
 533 reflections, as we anticipate that these will be the most widely used reflection properties. These GeoPackage files are a more
 534 openly accessible version of the MATLAB files, but include many fewer reflection properties due to limitations of the format.
 535 Reflection ages and age uncertainties are preserved in each GeoPackage file’s metadata. Table 5 describes the format of the
 536 NetCDF (.nc) file that contains the gridded (5 km horizontal resolution) isochrone depths and ages at normalized depths (§3.3,
 537 4). For brevity, in these three tables we describe only the key variables and not all preserved metadata or other attributes.

538 **Table 3:** Format of the “segment” structure in the MATLAB file for each campaign that contains the traced reflections at the radargram
 540 resolution.

Variable	Description	Units
----------	-------------	-------

Deleted: 14531734

Deleted: 4

Deleted: ,

name	Description	Units
name	Name of segment, including concatenated frames used	N/A
dist	Along-track distance, calculated using great circles and the WGS84 ellipsoid	m
lat	Latitude	°
lon	Longitude	°
num_layer	Number of traced reflections	N/A
num_trace	Number of traces in the concatenated segment	N/A
thick	Ice thickness	m
time	GPS measurement time since 0000-01-01	s
x	Projected x-coordinate, EPSG:3413	m
y	Projected y-coordinate, EPSG:3413	m
firm_corr	Modeled firm correction	m
stratigraphy	Structure with number of objects equal to num_layer that includes fields for each reflection property	N/A
stratigraphy.age	Reflection age	ka
stratigraphy.age_uncert	Uncertainty in reflection age	ka
stratigraphy.depth	Depth below ice surface to reflection (not corrected for firm)	m
stratigraphy.elev	Reflection elevation relative to WGS84 ellipsoid	m
stratigraphy.int	Reflection relative echo intensity (single sample, not window-integrated)	dB
stratigraphy.twtt	Englacial travelttime to reflection	s

544

545

Table 4: Format of GeoPackage files for each concatenated segment that contains the traced reflections at the radargram resolution.

Variable	Description	Units
geometry	Projected x- and y- coordinates, EPSG:3413	m
thick	Ice thickness	m
time	GPS measurement time since 0000-01-01	s

depth_XY.Z Depth below ice surface (not corrected for firm) to reflection whose age is X ka. If undated, the age is given as U. If more than one reflection is dated to that age (or undated), then the variable name is hyphenated with -0, -1 and so forth. m

Deleted: #

Deleted: (not corrected for firm)

546

547 **Table 5:** Format of NetCDF file that contains the gridded isochrone depths and ages at normalized depths.

Variable	Description	Units
x	Projected x-coordinate, EPSG:3413	m
y	Projected y-coordinate, EPSG:3413	m
age_iso	Ages of synthetic isochrones whose depth was gridded (depth, depthstd)	ka
age	Age at normalized depth	ka
agestd	Total uncertainty in age at normalized depth	ka
depth_norm	Thickness-normalized depths whose age was gridded (age, agestd)	%
depth	Isochrone depth	m
depthstd	Total uncertainty in isochrone depth	m

548

7 Conclusions

549 We produced a second version of a dated radiostratigraphic dataset covering a substantial portion (up to 65%) of the GrIS
 550 using a non-repeating subset of available NASA/NSF radargrams. While far from comprehensive, as innumerable minor
 551 reflections were left untraced – let alone dated – this dataset represents an improved and potentially large-scale constraint on
 552 models of the flow of the GrIS and their sensitivity to past climate change. The inferred basic age structure of the GrIS is not
 553 significantly changed from that which M15 first described, but its development was simplified and the resulting dataset has
 554 substantially fewer tracing errors, is more self-consistent and is expected to be more robust for future modeling efforts. This
 555 version of the dataset continues to indicate that the oldest ice in the Greenland is likely in northern central GrIS, that the ice
 556 sheet is significantly older in northeastern and far northern Greenland, and that the radiostratigraphy and age structure of the
 557 GrIS south of 65°N remains challenging to map using presently available data and techniques. Finally, we modernized and
 558 further generalized the tools used to generate this radiostratigraphy – as compared to the previous version of the dataset – and
 559 expect that they could be used to either improve upon this dataset in the future for the GrIS or to accelerate Antarctic-wide
 560 mapping of radiostratigraphy.

563 **Author contribution.** JAM, MAF and AA secured funding for this study. JAM performed most of the tracing and QC, led the
564 subsequent analysis, and drafted the manuscript. MAF aided in the analysis. JDP and JL processed the radar data. JPH traced
565 some of the radar data. All authors reviewed and edited the manuscript.

566 **Video supplement.** Movie S1 is available at both <https://doi.org/10.5281/zenodo.14531649> (MacGregor, 2024b) and also on
567 YouTube (<https://www.youtube.com/watch?v=eB0lVrQ0Awo>). Because of its size (3.3 GB), it is provided separate from the
568 dataset itself. This movie shows all 496 traced segments in chronological sequence, corrected for surface elevation as in Fig.
569 3e. A 50-km portion of each radargram is shown in each frame, which is translated by 20 km between each frame and is
570 recorded at 5 frames per second. Traced and dated reflections are shown in every other frame to enable visual evaluation of
571 the traced radiostratigraphy. An inset map of Greenland shows all traced segments, highlighting the current segment in blue
572 and the current frame in red. The color range of the displayed radargram is rescaled for each frame to the mean \pm two standard
573 deviations of the radargram amplitudes within that frame.

574 **Competing interests.** None declared.

575 **Acknowledgments.** We thank the NASA Cryospheric Sciences program for funding this study (solicitation
576 #NNH20ZDA001N) and the innumerable individuals who supported and performed the airborne surveys, ice-core drilling and
577 related work that ultimately made this study possible. We thank O. Eisen, N. B. Karlsson, E. J. MacKie, T. Rieckh and D.
578 Steinhage for valuable discussions.

579 **References**

- 580 Aschwanden, A., Fahnestock, M. A., Truffer, M., Brinkerhoff, D. J., Hock, R., Khroulev, C., Mottram, R., and Khan, S. A.:
581 Contribution of the Greenland Ice Sheet to sea level over the next millennium, *Sci. Adv.*, 5, eaav9396, [https://doi.org/](https://doi.org/10.1126/sciadv.aav9396)
582 [10.1126/sciadv.aav9396](https://doi.org/10.1126/sciadv.aav9396), 2019.
- 583 Aschwanden, A., Bartholomaeus, T. C., Brinkerhoff, D. J., Truffer, M.: Brief communication: A roadmap towards credible
584 projections of ice sheet contribution to sea level, *The Cryosphere*, 15, 5705–5715, <https://doi.org/10.5194/tc-15-5705-2021>,
585 2021.
- 586 Aschwanden, A. and Brinkerhoff, D. J.: Calibrated Mass Loss Predictions for the Greenland Ice Sheet, *Geophys. Res. Lett.*,
587 49, <https://doi.org/10.1029/2022gl099058>, 2022.
- 588 Bingham, R. G., Bodart, J. A., Cavitte, M. G. P., Chung, A., Sanderson, R. J., Sutter, J. C. R., Eisen, O., Karlsson, N. B.,
589 MacGregor, J. A., Ross, N., Young, D. A., Ashmore, D. W., Born, A., Chu, W., Cui, X., Drews, R., Franke, S., Goel, V.,
590 Goodge, J. W., Henry, A. C. J., Hermant, A., Hills, B. H., Holschuh, N., Koutnik, M. R., Leysinger Vieli, G. J.-M. C.,

Deleted: ¶

Formatted: Indent: Hanging: 0.13", Border: Top: (No border), Bottom: (No border), Left: (No border), Right: (No border), Between : (No border)

592 Mackie, E. J., Mantelli, E., Martin, C., Ng, F. S. L., Oraschewski, F. M., Napoleoni, F., Parrenin, F., Popov, S. V., Rieckh,
593 T., Schlegel, R., Schroeder, D. M., Siegert, M. J., Tang, X., Teisberg, T. O., Winter, K., Yan, S., Davis, H., Dow, C. F.,
594 Fudge, T. J., Jordan, T. A., Kulesa, B., Matsuoka, K., Nyqvist, C. J., Rahmounfar, M., Siegfried, M. R., Singh, S.,
595 Višnjević, V., Zamora, R., and Zuhr, A.: Review Article: Antarctica's internal architecture: Towards a radiostratigraphically-
596 informed age–depth model of the Antarctic ice sheets, *EGU*sphere [preprint], <https://doi.org/10.5194/egusphere-2024-2593>,
597 2024.

598 [Bodart, J. A., Bingham, R. G., Ashmore, D. W., Karlsson, N. B., Hein, A. S., and Vaughan, D. G.: Age-Depth Stratigraphy of](#)
599 [Pine Island Glacier Inferred From Airborne Radar and Ice-Core Chronology, *J. Geophys. Res.: Earth Surf.*, 126,](#)
600 <https://doi.org/10.1029/2020jf005927>, 2021.

601 Bons, P. D., Jansen, D., Mundel, F., Bauer, C. C., Binder, T., Eisen, O., Jessell, M. W., Llorens, M.-G., Steinbach, F.,
602 Steinhage, D. and Weikusat, I.: Converging flow and anisotropy cause large-scale folding in Greenland's ice sheet, *Nature*
603 *Commun.*, 7, 1–6, <https://doi.org/10.1038/ncomms11427>, 2016.

604 Born, A. and Robinson, A.: Modeling the Greenland englacial stratigraphy, *The Cryosphere*, 15, 4539–4556,
605 <https://doi.org/10.5194/tc-2020-355>, 2021.

606 Castelletti, D., Schroeder, D. M., Mantelli, E., and Hilger, A.: Layer optimized SAR processing and slope estimation in radar
607 sounder data, *J. Glaciol.*, 65, 983–988, <https://doi.org/10.1017/jog.2019.72>, 2019.

608 Cavitte, M. G. P., Young, D. A., Mulvaney, R., Ritz, C., Greenbaum, J. S., Ng, G., Kempf, S. D., Quartini, E., Muldoon, G.,
609 R., Paden, J., Frezzotti, M., Roberts, J. L., Tozer, C. R., Schroeder, D. M., and Blankenship, D. D.: A detailed
610 radiostratigraphic data set for the central East Antarctic Plateau spanning from the Holocene to the mid-Pleistocene, *Earth*
611 *Syst. Sci. Data*, 13, 4759–4777, <https://doi.org/10.5194/essd-13-4759-2021>, 2021.

612 Chu, W., Schroeder, D. M., Seroussi, H., Creyts, T. T., and Bell, R. E.: Complex Basal Thermal Transition Near the Onset of
613 Petermann Glacier, Greenland, *J. Geophys. Res.: Earth Surf.*, 123, 985–995, <https://doi.org/10.1029/2017jf004561>, 2018.

614 Cooper, M. A., Jordan, T. M., Schroeder, D. M., Siegert, M. J., Williams, C. N., and Bamber, J. L.: Subglacial roughness of
615 the Greenland Ice Sheet: relationship with contemporary ice velocity and geology, *The Cryosphere*, 13, 3093–3115,
616 <https://doi.org/10.5194/tc-13-3093-2019>, 2019.

617 Csatho, B. M., Schenk, A. F., Veen, C. J. van der, Babonis, G., Duncan, K., Rezvanbehbahani, S., Broeke, M. R. van den,
618 Simonsen, S. B., Nagarajan, S., and Angelen, J. H. van: Laser altimetry reveals complex pattern of Greenland Ice Sheet
619 dynamics, *Proc. Natl. Acad. Sci.*, 111, 18478–18483, <https://doi.org/10.1073/pnas.1411680112>, 2014.

620 Culberg, R. and Schroeder, D. M.: Simulations of Englacial Radiostratigraphy from ICE Core Measurements, 2021 IEEE Int.
621 Geosci. Remote Sens. Symp. IGARSS, 2943–2946, <https://doi.org/10.1109/igarss47720.2021.9553760>, 2021.

622 Dahl-Jensen, D., Albert, M. R., Aldahan, A., Azuma, N., Balslev-Clausen, D., Baumgartner, M., Berggren, A. M., Bigler, M.,
623 Binder, T., Blunier, T., Bourgeois, J. C., Brook, E. J., Buchardt, S. L., Buizert, C., Capron, E., Chappellaz, J., Chung, J.,
624 Clausen, H. B., Cvijanovic, I., Davies, S. M., Ditlevsen, P., Eicher, O., Fischer, H., Fisher, D. A., Fleet, L. G., Gfeller, G.,
625 Gkinis, V., Gogineni, S. P., Goto-Azuma, K., Grinsted, A., Gudlaugsdottir, H., Guillevic, M., Hansen, S. B., Hansson, M.

Deleted: ¶

Formatted: Line Number

Deleted: ¶

Formatted: Indent: Hanging: 0.13", Border: Top: (No border), Bottom: (No border), Left: (No border), Right: (No border), Between : (No border)

Deleted: ¶

629 E., Hirabayashi, M., Hong, S. M., Hur, S. D., Huybrechts, P., Hvidberg, C., Iizuka, Y., Jenk, T., Johnsen, S., Jones, T. R.,
630 Jouzel, J., Karlsson, N. B., Kawamura, K., Keegan, K., Kettner, E., Kipfstuhl, S., Kjær, H. A., Koutnik, M. R., Kuramoto,
631 T., Köhler, P., Laepple, T., Landais, A., Langen, P. L., Larsen, L. B., Leuenberger, D., Leuenberger, M., Leuschen, C. J.,
632 Li, J., Lipenkov, V. Y., Martinerie, P., Maselli, O. J., Masson-Delmotte, V., McConnell, J. R., Millar, D. H. M., Mini, O.,
633 Miyamoto, A., Montagnat-Rentier, M., Mulvaney, R., Muscheler, R., Orsi, A. J., Paden, J. D., Panton, C., Pattyn, F., Petit,
634 J.-R., Pol, K., Popp, T. J., Possnert, G., Prié, F., Prokopiou, M., Quiquet, A., Rasmussen, S. O., Raynaud, D., Ren, J. W.,
635 Reutenauer, C., Ritz, C., Röckmann, T., Rosen, J. L., Rubino, M., Rybak, O., Samyn, D., Sapart, C. J., Schilt, A., Schmidt,
636 A. M. Z., Schwander, J., Schüpbach, S., Seierstad, I., Severinghaus, J. P., Sheldon, S., Simonsen, S. B., Sjolte, J., Solgaard,
637 A. M., Sowers, T. A., Sperlich, P., Steen-Larsen, H. C., Steffén, K., Steffensen, J. P., Steinhage, D., Stocker, T. F., Stowasser,
638 C., Sturevik, A. S., Sturges, W. T., Sveinbjornsdottir, A. E., Svensson, A. M., Tison, J. L., Uetake, J., Vallelonga, P., van de
639 Wal, R. S. W., van der Wel, G., Vaughn, B. H., Vinther, B. M., Waddington, E. D., Wegner, A., Weikusat, I., White, J.,
640 Wilhelms, F., Winstrup, M., Witrant, E., Wolff, E. W., Xiao, C. D. and Zheng, J.: Eemian interglacial reconstructed from a
641 Greenland folded ice core, *Nature*, 493, 489–494, <https://doi.org/10.1038/nature11789>, 2013.

642 Das, I., Bell, R. E., Scambos, T. A., Wolovick, M., Creyts, T. T., Studinger, M., Frearson, N., Nicolas, J. P., Lenaerts, J. T.
643 M., and Broeke, M. R. van den: Influence of persistent wind scour on the surface mass balance of Antarctica, *Nat. Geosci.*,
644 6, 367–371, <https://doi.org/10.1038/ngeo1766>, 2013.

645 Delf, R., Schroeder, D. M., Curtis, A., Giannopoulos, A., and Bingham, R. G.: A comparison of automated approaches to
646 extracting englacial-layer geometry from radar data across ice sheets, *Ann. Glaciol.*, 61, 234–241,
647 <https://doi.org/10.1017/aog.2020.42>, 2020.

648 Dow, C. F., Karlsson, N. B. and Werder, M. A.: Limited Impact of Subglacial Supercooling Freeze-on for Greenland Ice Sheet
649 Stratigraphy, *Geophys. Res. Lett.*, 45, 1481–1489, <https://doi.org/10.1002/2017gl076251>, 2018.

650 Franke, S., Bons, P. D., Westhoff, J., Weikusat, I., Binder, T., Streng, K., Steinhage, D., Helm, V., Eisen, O., Paden, J. D.,
651 Eagles, G., and Jansen, D.: Holocene ice-stream shutdown and drainage basin reconfiguration in northeast Greenland, *Nat.*
652 *Geosci.*, 15, 995–1001, <https://doi.org/10.1038/s41561-022-01082-2>, 2022.

653 Franke, S., Bons, P. D., Streng, K., Mundel, F., Binder, T., Weikusat, I., Bauer, C. C., Paden, J. D., Dörr, N., Helm, V.,
654 Steinhage, D., Eisen, O., and Jansen, D.: Three-dimensional topology dataset of folded radar stratigraphy in northern
655 Greenland, *Sci. Data*, 10, 525, <https://doi.org/10.1038/s41597-023-02339-0>, 2023.

656 Franke, S., Steinhage, D., Helm, V., Zuhr, A. M., Bodart, J. A., Eisen, O., and Bons, P.: Age-depth distribution in western
657 Dronning Maud Land, East Antarctica, [and Antarctic-wide comparisons of internal reflection horizons](https://doi.org/10.5194/tc-19-1153-2025), *The Cryosphere*,
658 <https://doi.org/10.5194/tc-19-1153-2025>, 19, 1153–1180, 2025.

659 Goelzer, H., Nowicki, S., Edwards, T., Beckley, M., Abe-Ouchi, A., Aschwanden, A., Calov, R., Gagliardini, O., Gillet-
660 Chaulet, F., Gollledge, N. R., Gregory, J., Greve, R., Humbert, A., Huybrechts, P., Kennedy, J. H., Larour, E., Lipscomb,
661 W. H., clec’h, S. L., Lee, V., Morlighem, M., Pattyn, F., Payne, A. J., Rodehacke, C., Rückamp, M., Saito, F., Schlegel, N.,
662 Seroussi, H., Shepherd, A., Sun, S., Wal, R. van de, and Ziemann, F. A.: Design and results of the ice sheet model initialisation

Deleted: ¶

Formatted: Indent: Hanging: 0.13", Border: Top: (No border), Bottom: (No border), Left: (No border), Right: (No border), Between : (No border)

Deleted: ¶

Deleted: from three decades of radar surveys

Deleted: EGUsphere [preprint]

Deleted: [egusphere-2024-2349](https://doi.org/10.5194/tc-19-1153-2025)

Deleted: 4

669 experiments initMIP-Greenland: an ISMIP6 intercomparison, *The Cryosphere*, 12, 1433–1460, [https://doi.org/10.5194/tc-](https://doi.org/10.5194/tc-12-1433-2018)
670 12-1433-2018, 2018.

671 Goelzer, H., Nowicki, S., Payne, A., Larour, E., Seroussi, H., Lipscomb, W. H., Gregory, J., Abe-Ouchi, A., Shepherd, A.,
672 Simon, E., Agosta, C., Alexander, P., Aschwanden, A., Barthel, A., Calov, R., Chambers, C., Choi, Y., Cuzzone, J., Dumas,
673 C., Edwards, T., Felikson, D., Fettweis, X., Golledge, N. R., Greve, R., Humbert, A., Huybrechts, P., Le clec’h, S., Lee, V.,
674 Leguy, G., Little, C., Lowry, D. P., Morlighem, M., Nias, I., Quiquet, A., Rückamp, M., Schlegel, N.-J., Slater, D. A., Smith,
675 R. S., Straneo, F., Tarasov, L., van de Wal, R. and van den Broeke, M.: The future sea-level contribution of the Greenland
676 ice sheet: a multi-model ensemble study of ISMIP6, *The Cryosphere*, 14, 3071–3096, [https://doi.org/10.5194/tc-14-3071-](https://doi.org/10.5194/tc-14-3071-2020)
677 2020, 2020.

678 Hindmarsh, R. C. A., Leysinger-Vieli, G. J. -M. C., Raymond, M. J., and Gudmundsson, G. H.: Draping or overriding: The
679 effect of horizontal stress gradients on internal layer architecture in ice sheets, *J. Geophys. Res.*, 111, F02018,
680 <https://doi.org/10.1029/2005jf000309>, 2006.

681 Howat, I. M., Negrete, A. and Smith, B. E.: The Greenland Ice Mapping Project (GIMP) land classification and surface
682 elevation data sets, *The Cryosphere*, 8, 1509–1518, <https://doi.org/10.5194/tc-8-1509-2014>, 2014.

683 [Jansen, D., Franke, S., Bauer, C. C., Binder, T., Dahl-Jensen, D., Eichler, J., Eisen, O., Hu, Y., Kerch, J., Llorens, M.-G.,](#)
684 [Miller, H., Neckel, N., Paden, J., Riese, T. de, Sachau, T., Stoll, N., Weikusat, I., Wilhelms, F., Zhang, Y., and Bons, P. D.:](#)
685 [Shear margins in upper half of Northeast Greenland Ice Stream were established two millennia ago, *Nat. Commun.*, 15,](#)
686 [1193, <https://doi.org/10.1038/s41467-024-45021-8>, 2024.](#)

687 Jebeli, A., Tama, B. A., Janeja, V. P., Holschuh, N., Jensen, C., Morlighem, M., MacGregor, J. A., and Fahnestock, M. A.:
688 TSSA: Two-Step Semi-Supervised Annotation for Radargrams on the Greenland Ice Sheet, *IGARSS 2023 - 2023 IEEE Int.*
689 *Geosci. Remote Sens. Symp.*, 00, 56–59, <https://doi.org/10.1109/igarss52108.2023.10282880>, 2023.

690 Karlsson, N. B., Dahl-Jensen, D., Gogineni, S. P., and Paden, J. D.: Tracing the depth of the Holocene ice in North Greenland
691 from radio-echo sounding data, *Ann. Glaciol.*, 54, 44–50, <https://doi.org/10.3189/2013aog64a057>, 2013.

692 Karlsson, N. B., Schroeder, D. M., Sørensen, L. S., Chu, W., Dall, J., Andersen, N. H., Dobson, R., Mackie, E. J., Köhn, S. J.,
693 Steinmetz, J. E., Tarzona, A. S., Teisberg, T. O., and Skou, N.: A newly digitized ice-penetrating radar data set acquired
694 over the Greenland ice sheet in 1971–1979, *Earth Syst. Sci. Data*, 16, 3333–3344, [https://doi.org/10.5194/essd-16-3333-](https://doi.org/10.5194/essd-16-3333-2024)
695 2024, 2024.

696 Kjær, K. H., Larsen, N. K., Binder, T., Bjørk, A. A., Eisen, O., Fahnestock, M. A., Funder, S., Garde, A. A., Haack, H., Helm,
697 V., Houmark-Nielsen, M., Kjeldsen, K. K., Khan, S. A., Machguth, H., McDonald, I., Morlighem, M., Mouginot, J., Paden,
698 J. D., Waight, T. E., Weikusat, C., Willerslev, E. and MacGregor, J. A.: A large impact crater beneath Hiawatha Glacier in
699 northwest Greenland, *Sci. Adv.*, 4(11), <https://doi.org/10.1126/sciadv.aar8173>, 2018.

700 Krabill, W., Abdalati, W., Frederick, E., Manizade, S., Martin, C., Sonntag, J., Swift, R., Thomas, R., Wright, W., and Yungel,
701 J.: Greenland Ice Sheet: High-Elevation Balance and Peripheral Thinning, *Science*, 289, 428–430,
702 <https://doi.org/10.1126/science.289.5478.428>, 2000.

703 Leysinger-Vieli, G. J. M. C., Martin, C., Hindmarsh, R. C. A. and Lüthi, M. P.: Basal freeze-on generates complex ice-sheet
704 stratigraphy, *Nature Commun.*, 9, <https://doi.org/10.1038/s41467-018-07083-3>, 2018.

705 MacGregor, J. A., Fahnestock, M. A., Catania, G. A., Paden, J. D., Gogineni, S. P., Young, S. K., Rybarski, S. C., Mabrey,
706 A. N., Wagman, B. M. and Morlighem, M.: Radiostratigraphy and age structure of the Greenland Ice Sheet, *J. Geophys.*
707 *Res. Earth Surf.*, 120(2), 212–241, <https://doi.org/10.1002/2014jf003215>, 2015a.

708 MacGregor, J. A., Li, J., Paden, J. D., Catania, G. A., Clow, G. D., Fahnestock, M. A., Gogineni, S. P., Grimm, R., Morlighem,
709 M., Nandi, S., Seroussi, H. and Stillman, D. E.: Radar attenuation and temperature within the Greenland Ice Sheet, *J.*
710 *Geophys. Res.: Earth Surf.*, 120(6), 983–1008, <https://doi.org/10.1002/2014jf003418>, 2015b.

711 MacGregor, J. A., Colgan, W. T., Fahnestock, M. A., Morlighem, M., Catania, G. A., Paden, J. D., and Gogineni, S. P.:
712 Holocene deceleration of the Greenland Ice Sheet, *Science*, 351, 590–593, <https://doi.org/10.1126/science.aab1702>, 2016a.

713 MacGregor, J. A., Fahnestock, M. A., Catania, G. A., Aschwanden, A., Clow, G. D., Colgan, W. T., Gogineni, S. P.,
714 Morlighem, M., Nowicki, S. M. J., Paden, J. D., Price, S. F. and Seroussi, H.: A synthesis of the basal thermal state of the
715 Greenland Ice Sheet, *J. Geophys. Res.: Earth Surf.*, 121(7), 1328–1350, <https://doi.org/10.1002/2015jf003803>, 2016b.

716 MacGregor, J. A., Fahnestock, M. A., Colgan, W. T., Larsen, N. K., Kjeldsen, K. K., and Welker, J. M.: The age of surface-
717 exposed ice along the northern margin of the Greenland Ice Sheet, *J. Glaciol.*, 66, 667–684,
718 <https://doi.org/10.1017/jog.2020.62>, 2020.

719 MacGregor, J. A., Boisvert, L. N., Medley, B., Petty, A. A., Harbeck, J. P., Bell, R. E., Blair, J. B., Blanchard-Wrigglesworth,
720 E., Buckley, E. M., Christoffersen, M. S., Cochran, J. R., Csathó, B. M., De Marco, E. L., Dominguez, R. T., Fahnestock,
721 M. A., Farrell, S. L., Gogineni, S. P., Greenbaum, J. S., Hansen, C. M., Hofton, M. A., Holt, J. W., Jezek, K. C., Koenig, L.
722 S., Kurtz, N. T., Kwok, R., Larsen, C. F., Leuschen, C. J., Locke, C.D., Manizade, S. S., Martin, S., Neumann, T. A.,
723 Nowicki, S. M. J., Paden, J. D., Richter-Menge, J. A., Rignot, E. J., Rodríguez-Morales, F., Siegfried, M. R., Smith, B. E.,
724 Sonntag, J. G., Studinger, M., Tinto, K. J., Truffer, M., Wagner, T. P., Woods, J. E., Young, D. A. and Yungel, J. K.: The
725 scientific legacy of NASA's Operation IceBridge, *Rev. Geophys.*, 59, <https://doi.org/10.1029/2020RG000712>, 2021.

726 MacGregor, J. A., Chu, W., Colgan, W. T., Fahnestock, M. A., Felikson, D., Karlsson, N. B., Nowicki, S. M. J., and Studinger,
727 M.: GBaTSv2: a revised synthesis of the likely basal thermal state of the Greenland Ice Sheet, *The Cryosphere*, 16, 3033–
728 3049, <https://doi.org/10.5194/tc-16-3033-2022>, 2022.

729 MacGregor, J. A., Fahnestock, M. A., Paden, J. D., Li, J., Harbeck, J. P., and Aschwanden, A.: Dataset for: A revised and
730 expanded deep radiostratigraphy of the Greenland Ice Sheet from airborne radar sounding surveys between 1993–2019,
731 Zenodo, <https://doi.org/10.5281/zenodo.15132763>, 2025.

732 MacGregor, J. A.: joemacgregor/pickgui: Version 2.0.1, Submission version of PICKGUI/FENCEGUI/etc for v2 of Greenland
733 radiostratigraphy (v2.0.1). Zenodo, <https://doi.org/10.5281/zenodo.14183061>, 2024a.

734 MacGregor, J. A.: Supplementary Video (Movie S1) for Greenland radiostratigraphy v2 dataset (Version 1). Zenodo,
735 <https://doi.org/10.5281/zenodo.14531649>, 2024b.

Deleted: ¶

Formatted: Indent: Hanging: 0.13", Border: Top: (No border), Bottom: (No border), Left: (No border), Right: (No border), Between : (No border)

Deleted: ¶

Formatted: Indent: Hanging: 0.13", Border: Top: (No border), Bottom: (No border), Left: (No border), Right: (No border), Between : (No border)

Deleted: 14531734

Deleted: 4

740 MacKie, E. J., Field, M., Wang, L., Yin, Z., Schoedl, N., Hibbs, M., and Zhang, A.: GStatSim V1.0: a Python package for
741 geostatistical interpolation and conditional simulation, *Geosci. Model Dev.*, 16, 3765–3783, [https://doi.org/10.5194/gmd-](https://doi.org/10.5194/gmd-16-3765-2023)
742 16-3765-2023, 2023.

743 Medley, B., Neumann, T. A., Zwally, H. J., Smith, B. E., and Stevens, C. M.: Simulations of firn processes over the Greenland
744 and Antarctic ice sheets: 1980–2021, *The Cryosphere*, 16, 3971–4011, <https://doi.org/10.5194/tc-16-3971-2022>, 2022.

745 Mojtabavi, S., Wilhelms, F., Cook, E., Davies, S. M., Sinnl, G., Skov Jensen, M., Dahl-Jensen, D., Svensson, A., Vinther, B.,
746 M., Kipfstuhl, S., Jones, G., Karlsson, N. B., Faria, S. H., Gkinis, V., Kjær, H. A., Erhardt, T., Berben, S. M. P., Nisancioglu,
747 K. H., Koldtoft, I., and Rasmussen, S. O.: A first chronology for the East Greenland Ice-core Project (EGRIP) over the
748 Holocene and last glacial termination, *Climate of the Past*, 16, 2359–2380, <https://doi.org/10.5194/cp-16-2359-2020>, 2020.

749 Moqadam, H., and Eisen, O.: Review article: Feature tracing in radio-echo sounding products of terrestrial ice sheets and
750 planetary bodies, *EGUsphere*, <https://doi.org/10.5194/egusphere-2024-1674>, in review.

751 Moqadam, H., Steinhage, D., Wilhelm, A., and Eisen, O.: Going deeper with deep learning: automatically tracing internal
752 reflection horizons in ice sheets, *Machine Learning and Computation*,
753 [https://d197for5662m48.cloudfront.net/documents/publicationstatus/229337/preprint_pdf/b283884d4a95faa94a832b33ce7](https://d197for5662m48.cloudfront.net/documents/publicationstatus/229337/preprint_pdf/b283884d4a95faa94a832b33ce7e72d9.pdf)
754 [e72d9.pdf](https://d197for5662m48.cloudfront.net/documents/publicationstatus/229337/preprint_pdf/b283884d4a95faa94a832b33ce7e72d9.pdf), in review.

755 Morlighem, M., Williams, C. N., Rignot, E. J., An, L., Arndt, J. E., Bamber, J. L., Catania, G. A., Chauché, N., Dowdeswell,
756 J. A., Dorschel, B., Fenty, I., Hogan, K., Howat, I. M., Hubbard, A. L., Jakobsson, M., Jordan, T. M., Kjeldsen, K. K.,
757 Millan, R., Mayer, L., Mougnot, J., Noël, B. P. Y., O’Cofaigh, C., Palmer, S. J., Rysgaard, S., Seroussi, H., Siegert, M. J.,
758 Slabon, P., Straneo, F., Broeke, M. R. van den, Weinrebe, W., Wood, M. and Zinglens, K. B.: BedMachine v3: Complete
759 Bed Topography and Ocean Bathymetry Mapping of Greenland From Multibeam Echo Sounding Combined With Mass
760 Conservation, *Geophys. Res. Lett.*, 44, 11,051–11,061, <https://doi.org/10.1002/2017gl074954>, 2017.

761 Morlighem, M., Williams, C. N., Rignot, E. J., An, L., Arndt, J. E., Bamber, J. L., Catania, G. A., Chauché, N., Dowdeswell,
762 J. A., Dorschel, B., Fenty, I., Hogan, K., Howat, I. M., Hubbard, A. L., Jakobsson, M., Jordan, T. M., Kjeldsen, K. K.,
763 Millan, R., Mayer, L., Mougnot, J., Noël, B. P. Y., O’Cofaigh, C., Palmer, S. J., Rysgaard, S., Seroussi, H., Siegert, M. J.,
764 Slabon, P., Straneo, F., Broeke, M. R. van den, Weinrebe, W., Wood, M. and Zinglens, K. B.: IceBridge BedMachine
765 Greenland, Version 5, NASA National Snow and Ice Data Center Distributed Active Archive Center,
766 <https://doi.org/10.5067/VLJ5YXKCNXGO>, 2021.

767 Mougnot, J., Rignot, E. J., Bjørk, A. A., Broeke, M. R. van den, Millan, R., Morlighem, M., Noël, B., Scheuchl, B., and Wood,
768 M.: Forty-six years of Greenland Ice Sheet mass balance from 1972 to 2018, *Proc. Natl. Acad. Sci.*, 116 (19) 9239-9244,
769 <https://doi.org/10.7280/d1mm37>, 2019.

770 Nixdorf, U. and Göktas, F.: Spatial depth distribution of the subglacial bed and internal layers in the ice around NGRIP,
771 Greenland, derived with airborne RES, *J. Appl. Geophys.*, 175–182, [https://doi.org/10.1016/S0926-9851\(01\)00062-3](https://doi.org/10.1016/S0926-9851(01)00062-3), 2001.

772 Otosaka, I. N., Shepherd, A., Ivins, E. R., Schlegel, N.-J., Amory, C., Broeke, M. R. van den, Horwath, M., Joughin, I., King,
773 M. D., Krinner, G., Nowicki, S., Payne, A. J., Rignot, E., Scambos, T., Simon, K. M., Smith, B. E., Sørensen, L. S.,

Deleted: ¶

Formatted: Indent: Hanging: 0.13", Border: Top: (No border), Bottom: (No border), Left: (No border), Right: (No border), Between : (No border)

Deleted: ¶

Deleted: The Cryosphere Discuss.

Deleted: ¶

Deleted: ¶

Formatted: Indent: Hanging: 0.13", Border: Top: (No border), Bottom: (No border), Left: (No border), Right: (No border), Between : (No border)

779 Velicogna, I., Whitehouse, P. L., A. G., Agosta, C., Ahlström, A. P., Blazquez, A., Colgan, W., Engdahl, M. E., Fettweis,
780 X., Forsberg, R., Gallée, H., Gardner, A., Gilbert, L., Gourmelen, N., Groh, A., Gunter, B. C., Harig, C., Helm, V., Khan,
781 S. A., Kittel, C., Konrad, H., Langen, P. L., Lecavalier, B. S., Liang, C.-C., Loomis, B. D., McMillan, M., Melini, D.,
782 Mermild, S. H., Mottram, R., Mougino, J., Nilsson, J., Noël, B., Pattle, M. E., Peltier, W. R., Pie, N., Roca, M., Sasgen, I.,
783 Save, H. V., Seo, K.-W., Scheuchl, B., Schrama, E. J. O., Schröder, L., Simonsen, S. B., Slater, T., Spada, G., Sutterley, T.
784 C., Vishwakarma, B. D., Wesse, J. M. van, Wiese, D., Wal, W. van der, and Wouters, B.: Mass balance of the Greenland
785 and Antarctic ice sheets from 1992 to 2020, *Earth Syst. Sci. Data*, 15, 1597–1616, [https://doi.org/10.5194/essd-15-1597-](https://doi.org/10.5194/essd-15-1597-2023)
786 [2023](https://doi.org/10.5194/essd-15-1597-2023), 2023.

787 Nereson, N. A., Raymond, C. F., Waddington, E. D., and Jacobel, R. W.: Migration of the Siple Dome ice divide, West
788 Antarctica. *J. Glaciol.*, 44, 643–652, <https://doi.org/10.3189/s002214300000214>, 1998.

789 Parrenin, F., Hindmarsh, R. C. A., and Rémy, F.: Analytical solutions for the effect of topography, accumulation rate and
790 lateral flow divergence on isochrone layer geometry, *J. Glaciol.*, 52, 191–202,
791 <https://doi.org/10.3189/172756506781828728>, 2006.

792 Pantou, C.: Automated mapping of local layer slope and tracing of internal layers in radio echograms, *Ann. Glaciol.*, 55, 71–
793 77, <https://doi.org/10.3189/2014aog67a048>, 2014.

794 Pantou, C. and Karlsson, N. B.: Automated mapping of near bed radio-echo layer disruptions in the Greenland Ice Sheet, *Earth*
795 *Planet. Sci. Lett.*, 432(C), 323–331, <https://doi.org/10.1016/j.epsl.2015.10.024>, 2015.

796 Peng, C., Zheng, L., Liang, Q., Li, T., Wu, J., and Cheng, X.: ST-SOLOv2: Tracing Depth Hoar Layers in Antarctic Ice Sheet
797 from Airborne Radar Echograms with Deep Learning, *IEEE Trans. Geosci. Remote Sens.*,
798 <https://doi.org/10.1109/tgrs.2024.3480698>, 2024.

799 [Rasmussen, S. O., Andersen, K. K., Svensson, A. M., Steffensen, J. P., Vinther, B. M., Clausen, H. B., Siggaard-Andersen,](https://doi.org/10.1029/2005jd006079)
800 [M. -L., Johnsen, S. J., Larsen, L. B., Dahl-Jensen, D., Bigler, M., Röthlisberger, R., Fischer, H., Goto-Azuma, K., Hansson,](https://doi.org/10.1029/2005jd006079)
801 [M. E., and Ruth, U.: A new Greenland ice core chronology for the last glacial termination, *J. Geophys. Res.: Atmos.*, 111,](https://doi.org/10.1029/2005jd006079)
802 [D06102, <https://doi.org/10.1029/2005jd006079>, 2006.](https://doi.org/10.1029/2005jd006079)

803 Rieckh, T., Born, A., Robinson, A., Law, R., and Güllé, G.: Design and performance of ELSA v2.0: an isochronal model for
804 ice-sheet layer tracing, *Geosci. Model Dev.*, 17, 6987–7000, <https://doi.org/10.5194/gmd-17-6987-2024>, 2024.

805 [Rodríguez-Morales, F., Byers, K., Crowe, R., Player, K., Hale, R. D., Arnold, E. J., Smith, L., Gifford, C. M., Braaten, D.,](https://doi.org/10.1109/tgrs.2013.2266415)
806 [Pantou, C., Gogineni, S., Leuschen, C. J., Paden, J. D., Li, J., Lewis, C. C., Panzer, B., Alvestegui, D. Gomez-García, and](https://doi.org/10.1109/tgrs.2013.2266415)
807 [Patel, A.: Advanced Multifrequency Radar Instrumentation for Polar Research, *IEEE Trans. Geosci. Remote Sens.*, 52,](https://doi.org/10.1109/tgrs.2013.2266415)
808 [2824–2842, <https://doi.org/10.1109/tgrs.2013.2266415>, 2014.](https://doi.org/10.1109/tgrs.2013.2266415)

809 Seierstad, I. K., Abbott, P. M., Bigler, M., Blunier, T., Bourne, A. J., Brook, E., Buchardt, S. L., Buizert, C., Clausen, H. B.,
810 Cook, E., Dahl-Jensen, D., Davies, S. M., Guillevic, M., Johnsen, S. J., Pedersen, D. S., Popp, T. J., Rasmussen, S. O.,
811 Severinghaus, J. P., Svensson, A., and Vinther, B. M.: Consistently dated records from the Greenland GRIP, GISP2 and

Deleted: ¶

Formatted: Indent: Hanging: 0.13", Border: Top: (No border), Bottom: (No border), Left: (No border), Right: (No border), Between : (No border)

Deleted: ¶

Deleted: ¶

815 NGRIP ice cores for the past 104 ka reveal regional millennial-scale $\delta^{18}O$ gradients with possible Heinrich event imprint,
816 Quat. Sci. Rev., 106, 29–46, <https://doi.org/10.1016/j.quascirev.2014.10.032>, 2014.

817 Sime, L. C., Hindmarsh, R. C. A., and Corr, H.: Instruments and Methods Automated processing to derive dip angles of
818 englacial radar reflectors in ice sheets, J. Glaciol., 57, 260–266, <https://doi.org/10.3189/002214311796405870>, 2011.

819 Sime, L. C., Karlsson, N. B., Paden, J. D., and Gogineni, S. P.: Isochronous information in a Greenland ice sheet radio echo
820 sounding data set, Geophys. Res. Lett., 41, 1593–1599, <https://doi.org/10.1002/2013gl057928>, 2014.

821 Sullivan, C. and Kaszynski, A.: PyVista: 3D plotting and mesh analysis through a streamlined interface for the Visualization
822 Toolkit (VTK), J. Open Source Softw., 4, 1450, <https://doi.org/10.21105/joss.01450>, 2019.

823 [Sutter, J., Fischer, H., and Eisen, O.: Investigating the internal structure of the Antarctic ice sheet: the utility of isochrones for
824 spatiotemporal ice-sheet model calibration, The Cryosphere, 15, 3839–3860, <https://doi.org/10.5194/tc-15-3839-2021>,
825 \[2021\]\(#\).](#)

826 Winter, A., Steinhage, D., Arnold, E. J., Blankenship, D. D., Cavitte, M. G. P., Corr, H. F. J., Paden, J. D., Urbini, S., Young,
827 D. A., and Eisen, O.: Comparison of measurements from different radio-echo sounding systems and synchronization with
828 the ice core at Dome C, Antarctica, Cryosphere, 11, 653–668, <https://doi.org/10.5194/tc-11-653-2017>, 2017.

829 Xiong, S., Muller, J.-P., and Carretero, R. C.: A New Method for Automatically Tracing Englacial Layers from MCoRDS
830 Data in NW Greenland, Remote Sens., 10, 43, <https://doi.org/10.3390/rs10010043>, 2018.

Deleted: ¶

Formatted: Indent: Hanging: 0.13", Border: Top: (No border), Bottom: (No border), Left: (No border), Right: (No border), Between : (No border)

Deleted: ¶

Formatted: Indent: Hanging: 0.13", Border: Top: (No border), Bottom: (No border), Left: (No border), Right: (No border), Between : (No border)